An alternative AMSR2 vegetation optical depth for monitoring vegetation at large scales

Mengjia Wang, Lei Fan, Frédéric Frappart, Philippe Ciais, Rui Sun, Yi Liu, Xiaojun Li, Xiangzhuo Liu, Christophe Moisy, Wigneron J.-P.

An alternative AMSR2 vegetation optical depth for monitoring vegetation at large scales

Mengjia Wang[a,b,c], Lei Fan[d], Frédéric Frappart[c,e], Philippe Ciais[f], Rui Sun[a,b], Yi Liu[d], Xiaojun Li[c], Xiangzhuo Liu[c], Christophe Moisy[c], Jean-Pierre Wigneron[c,*]

a State Key Laboratory of Remote Sensing Science, Faculty of Geographical Science, Beijing Normal University, Beijing 100875, China

b Beijing Engineering Research Center for Global Land Remote Sensing Products, Faculty of Geographical Science, Beijing Normal University, Beijing 100875, China

c INRAE, UMR1391 ISPA, Université de Bordeaux, F-33140, Villenave d'Ornon, France

d School of Geographical Sciences, Nanjing University of Information Science and Technology, Nanjing, China

e Laboratoire d'Etudes en Géophysique et Océanographie Spatiales (LEGOS), 31400 Toulouse, French

f Laboratoire des Sciences du Climat et de l'Environnement, CEA/CNRS/UVSQ/Université Paris Saclay, Gif-sur-Yvette, France

*Corresponding Author: J.-P. Wigneron (jean-pierre.wigneron@inrae.fr)

Abstract:

Vegetation optical depth (VOD) retrieved from microwave observations has been found to be useful to monitor the dynamics of the vegetation features at global scale. Particularly, many applications could be developed in several fields of research (ecology, water and carbon cycle, etc.) from VOD products retrieved from the SMOS and SMAP observations at L-band, and from the combined AMSR-E (2002-2011) / AMSR2 (2012-present) observations at C- and X-bands. One of the main difficulties in retrieving VOD is that the microwave observations are sensitive to both the soil (mainly soil moisture) and vegetation (mostly VOD) features. The AMSR-E/2 sensors provide only mono-angular observations at two polarizations. These dual-channel observations may be strongly correlated so that retrieving SM and VOD simultaneously

can be an ill-posed problem. Here, to overcome this problem, we proposed and evaluated a new retrieval approach from AMSR2 observations at X-band to produce a new X-VOD product. The X-VOD retrievals were based on the inversion of the X-MEB model, an extension of the L-MEB model (L-band microwave emission of the biosphere) to the X-band. The main originality in comparison to previous algorithms is that (i) only VOD was retrieved while SM was estimated from a reanalysis data set (ERA5-Land); (ii) model inversion was based on an innovative approach to initialize the cost function; and (iii) new values for the soil and vegetation X-MEB model parameters were calibrated. To evaluate the methodology, we performed the VOD retrievals over the whole African continent over 2014-2016, including a dry (2015) and a wet (2014) year. In a first step, we calibrated a set of three parameters: effective scattering albedo (ω), soil roughness (H_R) and VOD first guess (VOD^{ini}). Several datasets of vegetation indices as Above-Ground Biomass (AGB), Leaf Area Index (LAI) and Normalized Difference Vegetation Index (NDVI) were chosen as reference data to optimize these model parameters. Globally-constant values ($\omega = 0.06$ and $H_R = 0.6$) were found to achieve high spatial and temporal correlations between retrieved X-VOD and the reference vegetation parameters. Comparison with other X-VOD products suggested IB X-VOD had competitive advantages in terms of both spatial and temporal performances. In particular, spatial correlation with three biomass datasets was found to be higher than for previous X-VOD products (R^2 ~ 0.76-0.83) and temporal correlation with LAI or NDVI showed obvious improvements, especially in dense vegetation.

Introduction:

Improved knowledge of the carbon, water and energy transformation between terrestrial surfaces and the atmosphere is essential for global climate and environment studies (Abbott et

al., 2019; Hamilton and Friess, 2018; Pan et al., 2017). Microwave remote sensing has helped in these research domains by providing global and long-term time series of vegetation properties. For example, Vegetation Optical Depth (VOD) is a useful proxy of vegetation water content (Feldman et al., 2018; Tian et al., 2018; Wigneron et al., 1995; Jackson and Schmugge, 1991), vegetation water status (Konings and Gentine, 2017; Konings et al., 2017a) or above-ground biomass (AGB) (Bastos et al., 2018; Brandt et al., 2018a; Fan et al., 2019; Liu et al., 2015; Tong et al., 2020; Wigneron et al., 2020, Qin et al., 2021).

VOD can be retrieved from microwave observations at different frequencies (L-VOD, C-VOD and X-VOD). As VOD is more sensitive to the features of the upper layers of vegetation as frequency increases (Li et al., 2021; Chaparro et al., 2019), different VOD indices can be used in a number of complementary applications (Frappart et al., 2020). The present study focuses on X-band observations from AMSR2 in consideration of: i) the higher sensitivity of C-band to radio frequency interference (RFI) at global scale (de Nijs et al., 2015; Draper, 2018; Lacava et al., 2012; Njoku et al., 2005); ii) the low penetration inside the vegetation cover at higher frequencies (K, Ka and W-bands). X-VOD products have been used in a number of applications: estimating the start of the vegetation growth and its annual variability at the ecoregion scale (Jones et al., 2012); detecting a recent reversal in loss of global terrestrial biomass from 2003 onwards (Liu et al., 2015); evaluating the degree of isohydricity at the ecosystem scale (Konings and Gentine, 2017); significantly improving the simulation of evapotranspiration and GPP (Kumar et al., 2020). These potential applications strengthen our motivations to extend the L-MEB (L-band microwave emission of the biosphere) model to X-band which offers a long-term observation records (AMSR-E & AMSR2). The X-MEB model is very similar to the L-MEB model, except that the soil and vegetation parameters of X-MEB need to be calibrated at X-band (Pellarin et al., 2006).

X-VOD data sets have been mainly retrieved from the LPDR algorithm (the Land Parameter Data Record) based on the inversion of the land-water emissivity slope index (Du et al., 2015; Du et al., 2017) and the LPRM (the Land Parameter Retrieval Model) algorithm based on the Microwave Polarization Difference Index (MPDI) (Owe et al., 2001; Owe et al., 2005; Owe et al., 2008). These algorithms were applied to observations from AMSR-E (the Advanced Microwave Scanning Radiometer for EOS, 2002-2011), AMSR2 (the Advanced Microwave Scanning Radiometer 2, 2012-present) and other satellites. For these sensors providing mono-angular observations, one difficulty may originate from the ill-posed problem for retrieving the parameters of interest: two parameters (SM and VOD) are retrieved from dual-polarized observations which are strongly correlated (Montpetit et al., 2015). Another important challenge is the large retrieval uncertainty of the X-VOD products in dense vegetation (>100 t/ha) (Du et al., 2017; Brandt et al., 2018a).

To overcome the first issue, several methods, such as use of a priori information (constraints) and multi-temporal algorithms, have been applied (Konings et al., 2016; Baur et al., 2019). As well, a recent study used the self-constrain relationship between soil and vegetation parameters as constraints (Zhao et al., 2021). In this study, we evaluated the possibility to retrieve VOD from AMSR2 using an approach similar to that applied in Baur et al. (2019), which consisted in retrieving only vegetation parameters while soil moisture (SM) was estimated from ancillary data. The observation time of the SM data derived from other Earth observation (EO) sensors (such as SMOS, SMAP) is different from that of AMSR2 and the time period of those products is too short (for instance, SMOS was launched in the end of 2009). Therefore, in the present study, we used model-based SM simulations from ECMWF ERA5-Land (C3S, 2019) as a known input. ERA5-Land is a state-of-the-art global reanalysis product that provides a long-term time series record at high spatial (~10 km) and temporal (hourly) resolutions. The use of modelled SM from ERA5-Land allowed having SM (and temperatures) data at exactly the same

time as the AMSR2 observations. Note that we evaluated in this study a new retrieval approach from AMSR2 observations at X-band, but our final objective is to compute eventually a long-term VOD time series from the AMSR-E/AMSR2 observations at both the C- and X-bands from 2002 to present.

In order to decrease the uncertainty on the retrieved VOD values, especially for dense vegetation, it is necessary to account for the effects of vegetation scattering, as parameterized by the effective scattering albedo (ω) and of soil roughness, as parameterized by the H_R parameter (Wigneron et al., 2017). The value of the effective scattering albedo is influenced by the vegetation type and structure (Kurum, 2013; Feldman et al., 2018) and there is significant variability in the value of ω across land cover classes (Konings et al., 2016). Previous studies generally assumed ω as polarization independent ($\omega_H = \omega_V$) and set ω to constant or to IGBP-land cover-class based values. Della Vecchia et al. (2009) and Baur et al. (2019) indicated a slight drop in ω with increasing frequencies. At X-band, Njoku et al. (2005) assumed vegetation scattering albedo to be negligible ($\omega = 0$) while Karthikeyan et al. (2019) set a globally fixed value equal to 0.06. LPDR (Du et al., 2015) and LPRM (Owe et al., 2001) used the same constant value. There are also some studies suggesting IGBP-based values, in the ranges of 0.03 to 0.08 (Gupta and Jangid, 2013), 0.05 to 0.1 (Baur et al., 2019), 0.06 to 0.12 (Pellarin et al., 2006). Similar to ω, the value of H_R at X-band is generally not consistent among different studies. Jackson (1993) assumed a constant H_R value of 0.1 at the global scale. Pellarin et al. (2006) found the optimum H_R value of 0.3 for various vegetation classes. Montpetit et al. (2015) calculated H_R from the standard deviation of measured soil height and obtained a range of 0 to 1.12. Karthikeyan et al., (2019) produced a H_R map with an even broader range of 0 to 3.5. The large range of values of ω and H_R at X-band found in the literatures showed the importance of implementing a complete calibration step of these two parameters for the X-MEB model in this study.

To perform the calibration step, some reference data were needed against which we could evaluate the X-VOD retrievals. VOD is a radiative transfer variable which is strongly related to the vegetation water content (VWC, kg/ m^2). However, estimating VWC is very difficult at large scales and it is a big challenge to validate VOD from coarse scale satellite observations in a direct way (Frappart et al., 2020; Li et al., 2021). Previous studies have suggested that VOD is strongly related to some reference variables of vegetation structure such as biomass (Wigneron et al., 2007; Tian et al., 2016; Santi et al., 2009; Liu et al., 2013; Liu et al., 2015; Brandt et al., 2018; Vittucci et al., 2019), LAI (Kerr et al., 2012; Kumar et al., 2020) and NDVI (O'Neill et al., 2015; Tian et al., 2016; Jones et al., 2012). Thus, in the present study, we used these three vegetation parameters (AGB, LAI and NDVI) to select the optimum parameters of (ω, H_R) in the X-VOD retrievals. The performance of the X-VOD parameter retrieved in this study (referred to as IB X-VOD, corresponding to AMSR2 INRAE Bordeaux X-Band VOD) was assessed by inter-comparing with other X-VOD products, including LPDR X-VOD (Du et al., 2015), VODCA X-VOD (VOD Climate Archive, Moesinger et al., 2020) and LPRM X-VOD (Owe et al., 2008).

The study is structured as follows: Section 2 introduces the datasets used in this study and the methodology presenting the new X-MEB model developed for the inversion of VOD at X-band, the calibration and inter-comparison steps. Section 3 presents the calibration results and the performances of the IB, LPDR, VODCA and LPRM X-VOD by comparison to vegetation proxies in time and space. Section 4 and 5 conclude with some remarks and perspectives.

Data and methodology

2.1 Data

The purpose of this study is to explore X-VOD retrievals based on AMSR2 observations using the X-MEB model. To this end, we selected the African continent which is large enough to

include a large variety in terms of vegetation and climate conditions, but not so large to allow analysing in detail a new methodology.

2.1.1 AMSR 2 brightness temperature

The AMSR2 sensor, on board the Global Change Observation Mission 1st-Water (GCOM-W) satellite which was launched by the Japan Aerospace Exploration Agency (JAXA) in May 2012, is a remote sensing instrument developed for accurately measuring the microwave emission from the land surface and the atmosphere of the Earth. It has a sun-synchronous orbit with an incidence angle of 55 degrees and a crossing time of 01:30/13:30±15 mins local standard time (LST), respectively, for the descending and ascending orbits.

AMSR2 measures the surface microwave emission from 7 frequency channels but we focused here on the X-band (10.65GHz) (https://suzaku.eorc.jaxa.jp/GCOM_W/data/data_w_index.html). The microwave signal at X-band has a ground spatial resolution of 24×42 km^2 at both vertical and horizontal polarizations. In consideration of the thermal equilibrium conditions of the near-surface air, canopy, and soil surface during night-time and as suggested by Owe et al. (2008), observations at 1:30 am LST, corresponding to the descending pass, were considered.

2.1.2 ERA5-Land

ERA5-Land is a global land surface reanalysis dataset, released by the European Centre for Medium-Range Weather Forecasts (ECMWF, https://cds.climate.copernicus.eu/), describing the land water and energy cycles. It is a downscaled land product from ERA5 (Hersbach et al., 2020) with a spatial resolution of 0.1°×0.1° (9 km) and a temporal resolution of one hour. Evaluation of ERA5-Land soil moisture against in situ measurements have suggested an overall good performance (Beck et al., 2020), and an acceptable uncertainty (ubRMSE = 0.05 m^3/m^3, Chen et al., 2021). In addition to SM, skin temperature, soil temperatures in 2 layers (0-7 cm

and 28-100 cm under the surface) were also used in X-MEB model. In order to keep datasets spatially consistent, ERA5-Land data was re-sampled to the grid of AMSR2 and to keep it temporally consistent with AMSR2 observations, ERA5-Land data simulated at 1:00 am was selected.

2.1.3 Vegetation variables used for validation

We selected three vegetation parameters, including AGB (Bouvet et al., 2018; Mermoz et al., 2015; Saatchi et al., 2011; Santoro et al., 2019), LAI, NDVI (Baret et al., 2007) to evaluate the retrieved IB X-VOD data. All the five vegetation parameters used here are based on optical, light detection and ranging (LiDAR) observations and Synthetic Aperture Radar (SAR) data from multiple Earth observation satellites and inventory datasets. They are thus completely independent of IB X-VOD, as the X-MEB model does not use any ancillary information on vegetation as presented above.

Saatchi AGB

Saatchi AGB was estimated from the Lorey's height (the basal area weighted height of all trees with a diameter of more than 10 cm). It was extracted based on Geoscience Laser Altimeter System (GLAS) (LiDAR) signal on NASA Ice, Cloud, and land Elevation (ICESat) satellite and spatially extrapolated with Moderate Resolution Imaging Spectroradiometer (MODIS) and Quick Scatterometer (QuikSCAT) data through maximum entropy (MaxEnt) modelling. The overall uncertainty in mapping AGB averaged over all continental regions is estimated at ±30% (Saatchi et al., 2011). Saatchi AGB map used in this study represents AGB circa 2015 year (Carreiras et al., 2017).

Bouvet-Mermoz AGB

Bouvet-Mermoz AGB (hereafter referred to as Bouvet AGB) consists of the merging of the Bouvet (Bouvet et al., 2018) and Mermoz (Mermoz et al., 2015) AGB datasets. Bouvet AGB

196 was produced using a Bayesian inversion of Phased Array L-band SAR (PALSAR) HH and
197 HV polarizations on Advanced Land Observing Satellite (ALOS) and evaluated with 144 field
198 plots collected between 2006 and 2012. Therefore, the resulting biomass dataset is
199 representative of AGB circa 2010. This dataset only focuses on savannahs and woodlands (low
200 biomass) in Africa at a spatial resolution of 25m × 25m. On the contrary, Mermoz et al. (2015)
201 paid more attention on the dense forest. Mermoz et al. used both theoretical and experimental
202 approaches to build a relationship between L-band SAR backscatter and dense tropical forest
203 biomass. Bouvet AGB has an overall good accuracy (RMSD = 17 $Mg \cdot ha^{-1}$) for the cross-
204 validation with the field plots (Bouvet et al., 2018).

205 **CCI AGB**

206 CCI AGB was produced by the European Space Agency's (ESA's) Climate Change Initiative
207 (CCI) programme (http://data.ceda.ac.uk/neodc/esacci/biomass/data/agb/maps/2017/v1.0/).
208 This data was derived based on L-band SAR observations (PALSAR-2) on ALOS-2 satellite
209 and C-band SAR observations on Sentinel-1 satellite (Santoro et al., 2019). The algorithm first
210 obtained growing stock volume (GSV), then converted to AGB with auxiliary datasets
211 describing canopy density, microwave transmissivity, maximum biomass etc. CCI AGB used
212 in this study is a global map for the year 2017.

213 **LAI and NDVI**

214 LAI and NDVI were downloaded from the Copernicus Global Land Service (CGLS) website
215 (https://land.copernicus.eu/global/). CGLS provides a series of bio-geophysical parameters
216 describing the vegetation dynamics at the global scale. These two products were derived from
217 PROBA-V since January 2014 onwards. LAI and NDVI both have a temporal resolution of 10
218 days and spatial resolution of 1 km. Quality control was conducted according to the reference

219 documents (Buchhorn et al., 2017; Swinnen et al., 2017). These datasets were resampled to a
220 spatial resolution of 25 km to keep them consistent with X-VOD.

221 **2.1.4 Other X-VOD products**

222 To assess the performance of the new X-VOD product retrieved in this study, we compared it
223 with three other X-VOD products, namely LPDR X-VOD (version 2), VOD Climate Archive
224 (VODCA X-band version 6), LPRM X-VOD (version 5), which are freely available to the
225 public.

226 LPDR X-VOD was designed by University of Montana (Du et al., 2015) based on LPDR
227 algorithm and is available at the National Snow & Ice Data Center (NSIDC) website
228 (https://nsidc.org/data/). LPDR provides a long-term (June 2002-present) global record of VOD
229 and other climate parameters at a 25km grid cell resolution (Du et al., 2017). The LPDR
230 algorithm is based on the (τ-ω) radiative transfer equation (Mo et al., 1982) and VOD is
231 retrieved by inverting a land-water emissivity slope index. It should be noted that LPDR regards
232 the soil as dry bare soil, therefore, LPDR X-VOD also incorporates surface roughness effects.
233 Importantly, note that the LPDR water fraction dataset was also used in the present study to
234 filter out pixels with large open water.

235 LPRM X-VOD was developed by Vrije Universiteit Amsterdam and NASA (Owe et al., 2008;
236 Owe et al., 2005; Owe et al., 2001) based on the Land Parameter Retrieval Model and is
237 available at the Goddard Earth Sciences Data and Information Services Center (GES DISC)
238 website (https://disc.gsfc.nasa.gov/datasets/). As for LPDR, the theoretical background is the τ-
239 ω model, but using MPDI to estimate the vegetation effects. LPRM relies on a nonlinear
240 iterative procedure to divide the emission signal into the soil part and the canopy part, and VOD
241 is retrieved in a second step.

VODCA was produced by Technische Universität Wien (Moesinger et al., 2020) and is available at https://doi.org/10.5281/zenodo.2575599. This product combines VOD retrievals that have been derived from multiple sensors (SSM/I, TMI, AMSR-E, WindSat and AMSR2) based on the LPRM model. To obtain a long-term and amplitude-consistent X-VOD, VODCA chose AMSR-E as the scaling reference and then applied a CDF-matching technique to adjust VOD from the other sensors. AMSR2 does not share any temporal overlap with the reference sensor, therefore, the scaled VOD from TMI was used to bridge this gap (Moesinger et al., 2020).

2.2 Methodology

In this study, VOD was retrieved by the inversion of the X-MEB model. The X-MEB model is an extension to the X-band of the L-MEB model which was defined by Wigneron (Wigneron et al., 2007; Wigneron et al., 2017) based on zero-order τ-ω radiative transfer model (Mo et al., 1982).

2.2.1 Radiative transfer theory

Radiative transfer model characterizes the complex process of microwave scattering and emission from different layers within the soil-vegetation media and finally sensed by the satellite antenna. In this study, we used the so-called τ-ω model and, as shown in (Kurum et al., 2013; Li et al., 2020), using higher-order solutions of the radiative transfer solution did not improve VOD retrievals. In the τ-ω model, the upwelling radiation (brightness temperature at polarization P (TB_P)) as observed from above the canopy consists of three components: 1) the radiation from the soil layer attenuated by the overlaying vegetation; 2) the upward radiation from the vegetation; and 3) the downward radiation from the vegetation, reflected upwards by the soil layer again (Mo et al., 1982; Paloscia et al., 1993; Fujii et al., 2009; Yang et al., 2007):

$$TB_P = (1 - r_{GP})\gamma_P T_G + (1 - \omega)(1 - \gamma_P)T_C + (1 - \omega)(1 - \gamma_P)r_{GP}\gamma_P T_C \quad (1)$$

with $\gamma_P = exp\left(\frac{-VOD}{cos\theta}\right)$ (2)

where P denotes the horizontal (P = H) or vertical (P = V) polarization; θ denotes the incidence angle; T_G and T_C represent, respectively, the effective temperature of soil and vegetation; ω denotes the effective scattering albedo of vegetation; r_{GP} is the soil reflectivity at polarization (P) which is related to soil moisture, soil texture, soil roughness (H_R) and the incidence angle (θ) (Njoku and Kong, 1977; Choudhury et al., 1979; Schmugge and Choudhury, 1981; Yang et al., 2005; Koike, 1996); γ_P represents the soil signal attenuation by the vegetation canopy with the assumption of isotropic conditions and no dependence on the polarization ($\gamma_H = \gamma_V$). The vegetation attenuation is determined by biomass, vegetation moisture content (%), vegetation structure and is usually described as a function of the vegetation optical depth at nadir (VOD) and the incidence angle (θ) as in Eq. (2). VOD has been considered as a good proxy of biomass and vegetation water content (Li et al., 2021; Chaparro et al., 2019; Frappart et al., 2020). VOD = 0, means the measured signal comes only from the soil (at X-band the signal from the atmosphere can be neglected generally). On the contrary, the soil signal is completely attenuated for very high VOD values (*i.e.* over dense vegetation). The absolute magnitude of brightness temperature at V polarization is somewhat higher than at H polarization. The difference of the emissivity from the land surface between the H and V polarizations decreases with gradually denser vegetation, eventually to almost zero for very dense vegetation (Owe et al., 2001). In consideration of the above characteristics, the polarization ratio, also termed as the microwave polarization difference index (MPDI = (TB_V - TB_H) / (TB_V +TB_H)) is a good indicator of the canopy density (Becker et al., 1998; Owe et al., 2001; Shi et al., 2008) and it will be analysed in detail in section 2.2.2.

2.2.2 X-MEB Model

In this study, we used the X-MEB model to exclusively retrieve VOD, while ERA5-Land SM (0-7 cm) was considered as a known input. In the X-MEB model, the key part is to clarify the details of the input parameters: the effective soil and vegetation temperatures (T_G and T_C), and the soil (r_{GP}) and vegetation (γ_P and ω) parameters.

T_G represents the effective soil temperature. It presents gradients within soil which emphasizes the necessity to consider temperatures in different layers to compute T_G. Choudhury et al. (1982) developed an effective soil temperature equation as a function of temperatures in different layers, soil dielectric constant and the observation wavelength. Wigneron et al. (1995, 2008) refined the equation by considering soil moisture and soil texture. More detailed and complete information on the calculation of T_G in X-MEB model can be found in Wigneron et al. (2007) and Wigneron et al. (2008). As in SMOS-IC (Wigneron et al., 2021), ERA5-Land soil temperature in the 0-7 cm and 28-100 cm top soil layers, and ERA5-Land skin temperature were used to compute, respectively, the effective temperature of soil (T_G) and of vegetation (T_C);

The reflectivity of soil (r_{GP}) is computed as a function of the reflectivity of a smooth soil (r^*_{GP}), the soil roughness parameter (H_R) and the incidence angle (θ):

$$r_{GP} = r^*_{GP} \, exp(-H_R \times cos\theta) \quad (3)$$

As only observations at H polarization at one angle were modelled with X-MEB, only one roughness parameter (H_R) was used in this study. The reflectivity (r^*_{GP}) of a smooth soil was calculated using the Fresnel coefficients (Ulaby et al., 1986) as a function of the effective soil dielectric constant (ε) and the incidence angle (θ). As in L-MEB, the Mironov model (Mironov et al., 2012) was also used in the X-MEB model to compute the soil dielectric constant as a function of soil temperature (T_G), soil moisture (SM) and the percentage of clay.

As for the vegetation parameters, γ_P represents the soil signal attenuation by the vegetation determined by VOD and the incidence angle (θ) as given in Eq. (2). ω denotes the effective scattering albedo of vegetation which needs to be calibrated in this study.

The AMSR2 TB observations were simulated using Eq. (1-3) and VOD was retrieved by the inversion of the X-MEB model. An iterative method was used to determine the minimum value of the cost function below (Wigneron et al., 2017):

$$cost\ function = \frac{({TB_P}^{obs} - {TB_P}^{sim})^2}{\sigma(TB)^2} + \frac{(VOD^{ini} - VOD^{ret})^2}{\sigma(VOD)^2} \quad (4)$$

Where TB_P^{obs} and TB_P^{sim} denote, respectively, the observed and simulated brightness temperature at the P polarization; VOD^{ini} and VOD^{ret} represent, respectively, the initial and the retrieved VOD; σ(TB) and σ(VOD) are the standard deviation of, respectively, the brightness temperature and VOD. When the initial VOD (VOD^{ini}) is considered as reliable, a strong constraint (low σ(VOD) value) is generally used; on the contrary, if there is a high uncertainty associated with VOD^{ini}, a weak constraint (high σ(VOD) value) is chosen. VOD^{ini} and σ(VOD) were calibrated as presented in the next section. Note that here, contrary to the SMOS-IC retrieval at L-band which considers both polarizations simultaneously in the cost function, we used only observations at H polarization in the cost function (this specific choice was made after many tests evaluating the retrieval performance; not shown here). The observations at both the H and V polarizations were used to estimate VOD^{ini}, as presented below.

2.2.3 Calibration

In this study, the IB X-VOD retrieval is based on the minimization of Eq. (4). In a preliminary step, two vegetation and soil parameters (ω and H_R) and two retrieval parameters (VOD^{ini} and σ(VOD)) have to be calibrated. The parameters were divided into 2 groups (group 1: ω and H_R, group 2: VOD^{ini} and σ(VOD)). These 2 groups were calibrated alternately, following an

iterative calibration process (Fig. 2). We stopped the calibration when the values of the optimized parameters were the same as those from the last step. Convergence was obtained very quickly (after 2 rounds generally) as shown below. It should be noted that the pixels which were considered polluted by water bodies (if water fraction >5%) were filtered out in this study. Calibration was made considering only one year (2016), while evaluation was made over three years (2014-2016).

Calibration of the effective vegetation scattering albedo (ω) and of soil roughness (H_R)

Previous studies suggest the effective vegetation scattering albedo is related to the vegetation classes, leaf structure, phenology and microwave frequency (Pampaloni and Paloscia, 1986; Della Vecchia et al., 2009; Kurum, 2013; Wigneron et al., 2004; Baur et al., 2019; Zhang et al., 2019). As presented in introduction, in order to simplify the radiative transfer model, most previous studies consider ω as independent on polarization and use different constant values at the global scale (Njoku et al., 2005; Owe et al., 2008; Du et al., 2015). There are also some researches suggesting IGBP-land cover based values (Gupta and Jangid, 2013; Baur et al., 2019; Pellarin et al., 2006). Similarly, there is little consistency in the value of the soil roughness parameter H_R at X-band (Jackson,1993; Pellarin et al., 2006; Montpetit et al., 2015; Karthikeyan et al., 2019). On account of the uncertainty in the value of H_R and ω, it was necessary to calibrate these parameters in the X-MEB model. To do so, in a first step, we considered VOD^{ini} as unknown (VOD^{ini} was set arbitrary to 0.5) and considered that a large uncertainty was associated with this value and we thus used a weak constraint ($\sigma(VOD) = 0.5$). The tested values of ω and H_R were as follows:

$\omega = \{0.05, 0.06, 0.07\}$;

$H_R = \{0.2, 0.4, 0.6, 0.8, 1.0\}$;

Note that the variation intervals are relatively narrow, because they were already shortened after some preliminary tests (not shown here to focus on the main results of the calibration step).

Evaluating and assessing the performance of the VOD retrievals is essential for improving its accuracy and exploring its potential applications in many fields such as monitoring global biomass (Liu et al., 2013; Liu et al., 2015; Hornbuckle et al., 2016), GPP (Teubner et al., 2018; Teubner et al., 2019; Kumar et al., 2020), vegetation dynamics (Liu et al., 2018; Zhou et al., 2018), crop yields (Guan et al., 2017; Chaparro et al., 2018; Mateo-Sanchis et al., 2019), phenology (Jones et al., 2011; Tong et al., 2019) and drought (Rao et al., 2019). However, VOD, as a radiometric variable, is neither well-defined nor easily-validated (Liu et al., 2011). Therefore, it is not possible to validate VOD at a continental scale in a direct way because of the limitation of reference values from in-situ measurements or models (Li et al., 2021). Previous studies suggest that there are strong relationships in time and space between X-VOD and some reference variables such as biomass (Wigneron et al., 2007; Tian et al., 2016; Santi et al., 2009; Liu et al., 2013; Liu et al., 2015; Vittucci et al., 2019), LAI (Kerr et al., 2012; Kumar et al., 2020) and NDVI (O'Neill et al., 2015; Tian et al., 2016; Jones et al., 2012). Accordingly, comparing VOD with these related parameters is an alternative and indirect way to evaluate the VOD performances which has often been used (Fernandez-Moran et al., 2017; Rodríguez-Fernández et al., 2018). Note that the main limitation of that type of evaluation may arise from time lags between different vegetation indices which are not related to exactly the same dynamic vegetation features (biomass, water content, LAI, etc.) (Jones et al., 2014; Tian et al., 2018, Li et al., 2021).

In the calibration step, to evaluate the retrieved VOD values, we considered both spatial and temporal correlations. More precisely, during 2016, we computed (i) the spatial correlation (coefficient of determination, R^2) between yearly average values of retrieved VOD and LAI, NDVI, and AGB (Saatchi, Bouvet-Mermoz, CCI) and (ii) the temporal correlation (Pearson's

correlation coefficient, R) between 10-day retrieved VOD and LAI or NDVI for each pixel. Note that the temporal correlation was computed only for pixels where the maximum value of LAI exceeded 0.5 in order to remove non-vegetation areas. The optimized values of ω and H_R were selected when they provided the highest values in terms of spatial and temporal correlations. A priority list was used to select most important criteria: spatial correlation > temporal correlation and Biomass > LAI > NDVI. This means that in the present study we put more emphasis on retrieving a VOD product which is a good proxy of biomass. Results we obtained in terms of temporal correlation showed fewer variations than those obtained in terms of spatial correlation for the tested parameters. Therefore, we only set a minimum threshold (R > 0.6) for temporal R. If this latter condition was satisfied, we focused on spatial correlation. This method will also be used in the following (second step) calibration work.

Calibration of two retrieval parameters VOD^{ini} and σ(VOD)

After calibrating ω and H_R, in a second step, we calibrated VOD^{ini} and σ(VOD). Many studies have indicated MPDI could be a potential variable for the retrieval of VOD (Pampaloni and Paloscia, 1985; Paloscia and Pampaloni, 1988; Paloscia and Pampaloni, 1992; Becker and Choudhury, 1988; Koike et al., 2004; Owe et al., 2008; Meesters et al., 2005) and have suggested a decreasing trend of VOD with increasing values of MPDI. However, the literature provided no clear information on the changing rate of the MPDI/VOD relationship and on the VOD value for very low MPDI value (~ the intercept). In this study, we estimated VOD^{ini} from MPDI using a simple exponential equation based on two parameters (intercept and slope); intercept being considered as a constant. The latter assumptions were derived from an analysis of the above-mentioned literature results and led to the following equation:

$$VOD^{ini} = intercept \times exp(slope \times MPDI) \quad (5)$$

where intercept is a value corresponding to very low MPDI values that are associated to very dense vegetation and thus to very high VOD values. We tested different values of the slope while the intercept was set to a constant value (Fig. 1). The latter value was computed as follows: i) from the first step of calibration, the optimum values of ω and H_R were obtained; ii) the corresponding VOD value was further retrieved; iii) the 95th percentile of VOD (VOD95) value in Africa was computed and set as the intercept (VOD95 = 1.1). An iterative analysis of the retrieved intercept value confirmed that this setting was optimal.

In this second step, ω and H_R were set to the optimized values obtained in the first step. Constant slope and σ(VOD) were used over all pixels, while VOD^{ini} had strong spatio-temporal variations which were related to the MPDI values. The tested values of slope and σ(VOD) were as follows:

slope = {-20, -40, -80, -160, -320};

σ(VOD) = {0.025, 0.05, 0.1, 0.2, 0.3, 0.4, 0.5};

Intercept = 1.1;

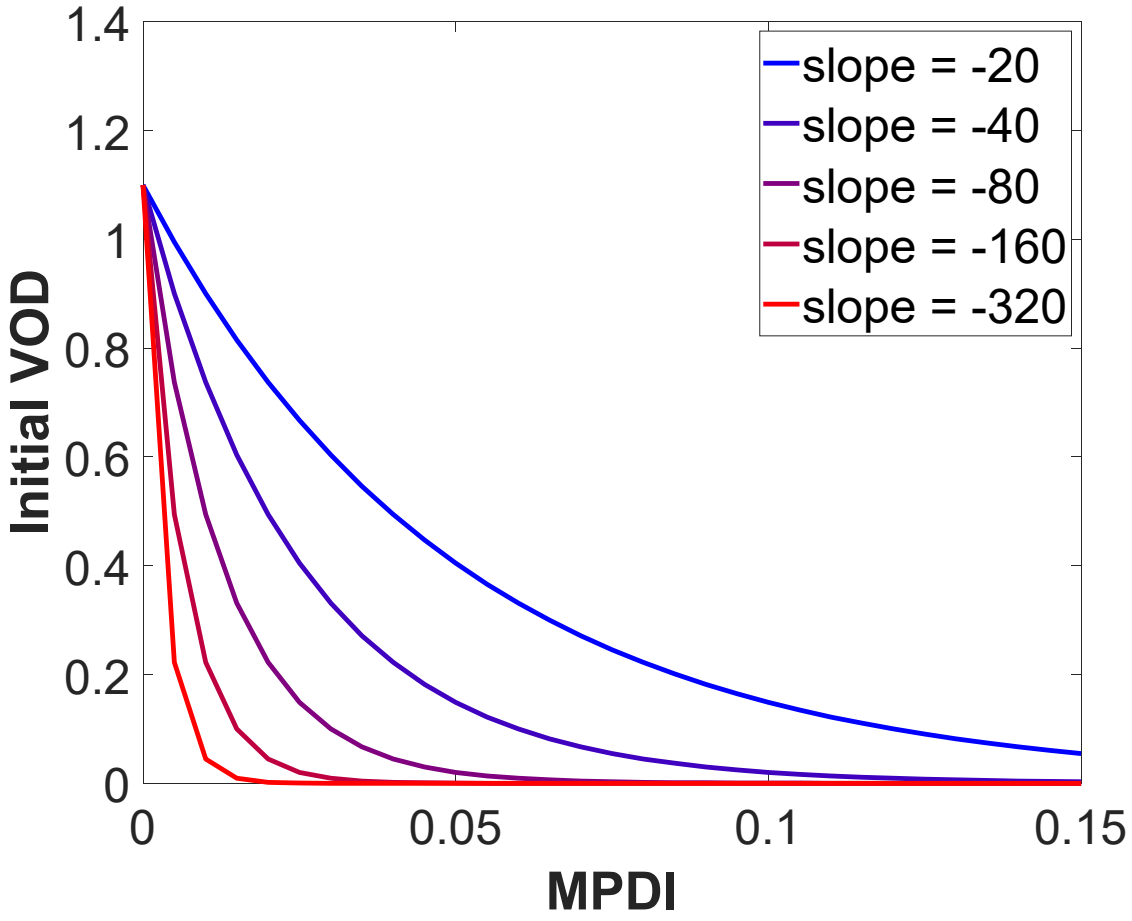

422

423 **Fig. 1.** Initial VOD (VOD^{ini}) written as an exponential function of MPDI.

424 **Iterative calibration**

425 At the end of the second step of calibration, we obtained the optimized values of ω, H_R, VOD^{ini}
426 and σ(VOD). As (ω, H_R) and (VOD^{ini}, σ(VOD)) were calibrated separately, it was necessary to
427 perform an iterative analysis to finalize these calibrated values. Thus, we used the obtained
428 values and performed again the first and second step described above until a convergence was
429 obtained in the calibrated values. In this iterative process, as the sensitivity of the results to H_R
430 was low, we set H_R to the constant value of 0.6 obtained during the first iteration. Convergence
431 in this iterative process was obtained quickly (after two rounds generally). Fig. 2 illustrates the
432 flow chart of the whole methodology, including the input data (blue rectangles), the calibration
433 step (green rectangles) and the comparison step (red rectangles). In the evaluation part, we

extended the study period to 3 years (from year 2014 to 2016) including a dry year (2015) and a wet year (2014) to ensure making the calibration for a large range of climatic conditions. We compared IB X-VOD with the other X-VOD products (LPDR X-VOD, VODCA X-VOD and LPRM X-VOD) by calculating the spatial correlation with the Bouvet/Saatchi/CCI AGB datasets, LAI and NDVI and the temporal correlation with LAI and NDVI (as we did in the calibration part). Only the pixels where these four VOD products were available were considered in the VOD inter-comparison step.

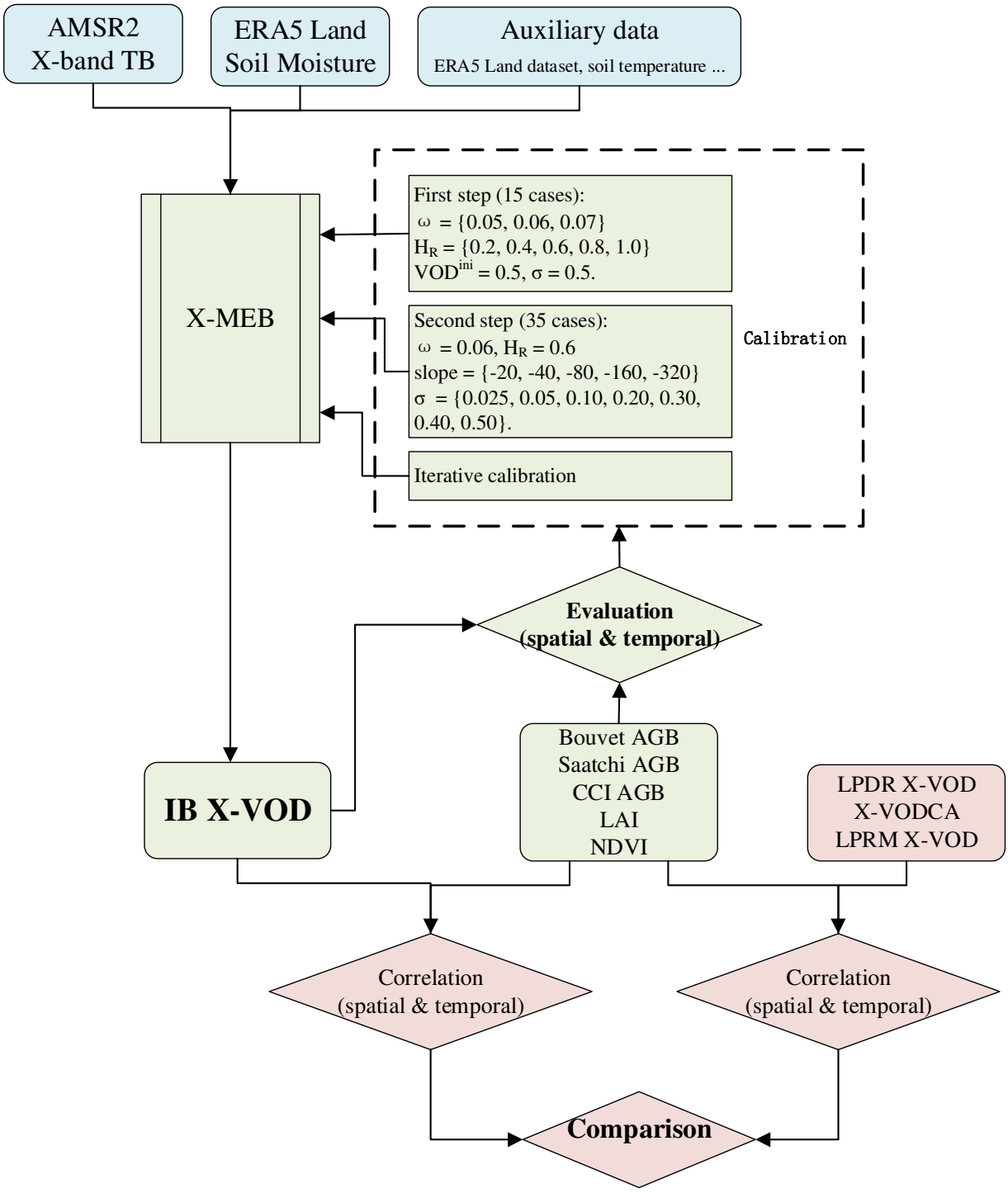

441

442 **Fig. 2.** Flow chart presenting the retrieval algorithm of IB X-VOD from AMSR2.

Results

3.1 Calibration

3.1.1 First step: Calibration of the effective vegetation scattering albedo and soil roughness

This section presents the results from the first step which focused on the calibration of the effective vegetation scattering albedo (ω) and soil roughness (H_R). Fig. 3 presents the spatial and temporal correlation with independent datasets (Bouvet/ Saatchi/ CCI AGB, LAI and NDVI) obtained for several combinations of the values of ω and H_R, assumed to be constant over the whole study area (Africa). It can be seen that the values of ω and H_R which produced the highest spatial correlation values are not quite consistent with those producing the highest temporal correlation values. It can also be seen that for a given value of ω, changes in H_R have a relatively small impacts on the results. The values ω = 0.06, H_R = 0.6 which were estimated to be optimum values in terms of spatial correlation, were also found to be relatively satisfying in terms of temporal correlation, so we selected them in this first step.

(a) Spatial R^2 with Bouvet AGB

ω \ H_R	0.2	0.4	0.6	0.8	1
0.05	0.617	0.614	0.611	0.609	0.608
0.06	0.678	0.678	0.677	0.675	0.673
0.07	0.582	0.598	0.611	0.623	0.635

(b) Spatial R^2 with Saatchi AGB

ω \ H_R	0.2	0.4	0.6	0.8	1
0.05	0.506	0.503	0.499	0.497	0.495
0.06	0.583	0.582	0.58	0.576	0.573
0.07	0.489	0.506	0.52	0.532	0.543

458

(c) Spatial R^2 with CCI AGB

ω \ H_R	0.2	0.4	0.6	0.8	1
0.05	0.604	0.601	0.598	0.596	0.595
0.06	0.669	0.669	0.667	0.663	0.661
0.07	0.590	0.604	0.617	0.627	0.634

(d) Spatial R^2 with LAI

ω \ H_R	0.2	0.4	0.6	0.8	1
0.05	0.748	0.747	0.746	0.745	0.745
0.06	0.779	0.779	0.777	0.775	0.774
0.07	0.741	0.748	0.754	0.759	0.762

459

(e) Spatial R^2 with NDVI

ω \ H_R	0.2	0.4	0.6	0.8	1
0.05	0.861	0.865	0.866	0.866	0.864
0.06	0.862	0.867	0.871	0.87	0.869
0.07	0.848	0.855	0.86	0.863	0.863

460

(f) Temporal R with LAI

ω \ H_R	0.2	0.4	0.6	0.8	1.0
0.05	0.668	0.671	0.675	0.679	0.683
0.06	0.654	0.658	0.663	0.667	0.672
0.07	0.634	0.641	0.648	0.654	0.661

(g) Temporal R with NDVI

ω \ H_R	0.2	0.4	0.6	0.8	1.0
0.05	0.632	0.634	0.637	0.640	0.642
0.06	0.620	0.624	0.627	0.630	0.634
0.07	0.601	0.606	0.611	0.616	0.622

461 **Fig. 3.** First step of calibration: spatial correlation (R^2) between IB X-VOD and Bouvet AGB
462 (a), Saatchi AGB (b), CCI AGB (c), LAI (d) and NDVI (e) and temporal correlation (R)
463 between IB X-VOD and LAI (f), NDVI (g) for different values of (ω, H_R); Red > Orange >
464 Yellow > light green > green > dark green represents the code of colours from the highest R
465 values to the lowest R values.

3.1.2 Second step: Calibration of VOD^{ini}

To calibrate VOD^{ini} during this 2nd step, we set $\omega = 0.06$ and $H_R = 0.6$ as optimized from the first step and tested different values of slope and σ(VOD). In general, slope and σ(VOD) had both substantial impacts on VOD (Fig. 4). Optimum values of (slope, σ(VOD)) for spatial correlation were found in the top-left corner of the tables, while they were found in the lower-right corner of the tables for temporal correlations. Taken all together, we considered σ(VOD) = 0.1 and slope = -40 as the optimum values for spatial calibration. These values which correspond to relatively good values in terms of temporal correlations were selected in this 2nd step.

(a) Spatial R^2 with Bouvet AGB

σ(VOD) \ Slope	-20	-40	-80	-160	-320
0.025	0.801	0.810	0.736	0.609	0.742
0.05	0.799	0.811	0.754	0.622	0.738
0.1	0.805	0.814	0.793	0.661	0.671
0.2	0.792	0.808	0.816	0.798	0.683
0.3	0.765	0.788	0.802	0.800	0.742
0.4	0.742	0.766	0.782	0.786	0.763
0.5	0.674	0.687	0.700	0.770	0.761

(b) Spatial R^2 with Saatchi AGB

σ(VOD) \ Slope	-20	-40	-80	-160	-320
0.025	0.758	0.755	0.632	0.465	0.671
0.05	0.757	0.757	0.661	0.510	0.688
0.1	0.753	0.757	0.721	0.584	0.642
0.2	0.725	0.739	0.743	0.719	0.597
0.3	0.686	0.709	0.720	0.717	0.655
0.4	0.653	0.679	0.694	0.697	0.674
0.5	0.565	0.579	0.592	0.676	0.666

(c) Spatial R^2 with CCI AGB

σ(VOD) \ Slope	-20	-40	-80	-160	-320
0.025	0.821	0.820	0.714	0.608	0.750
0.05	0.822	0.822	0.736	0.625	0.743
0.1	0.820	0.825	0.788	0.662	0.654
0.2	0.796	0.811	0.813	0.789	0.648
0.3	0.763	0.784	0.793	0.787	0.722
0.4	0.735	0.758	0.770	0.771	0.747
0.5	0.653	0.668	0.679	0.753	0.742

(d) Spatial R^2 with LAI

σ(VOD) \ Slope	-20	-40	-80	-160	-320
0.025	0.863	0.873	0.821	0.812	0.805
0.05	0.866	0.879	0.836	0.819	0.804
0.1	0.873	0.885	0.866	0.804	0.743
0.2	0.855	0.872	0.872	0.839	0.725
0.3	0.834	0.852	0.857	0.846	0.799
0.4	0.816	0.834	0.841	0.838	0.819
0.5	0.765	0.776	0.782	0.827	0.817

478

(e) Spatial R^2 with NDVI					
Slope / σ(VOD)	-20	-40	-80	-160	-320
0.025	0.806	0.866	0.837	0.815	0.693
0.05	0.817	0.884	0.843	0.797	0.662
0.1	0.867	0.899	0.868	0.794	0.699
0.2	0.889	0.896	0.885	0.855	0.809
0.3	0.888	0.890	0.885	0.873	0.853
0.4	0.884	0.886	0.883	0.876	0.867
0.5	0.862	0.866	0.867	0.877	0.871

479

(f) Temporal R with LAI					
Slope / σ(VOD)	-20	-40	-80	-160	-320
0.025	0.510	0.524	0.544	0.478	0.344
0.05	0.507	0.537	0.556	0.515	0.400
0.1	0.523	0.601	0.608	0.555	0.477
0.2	0.588	0.654	0.690	0.689	0.671
0.3	0.616	0.663	0.691	0.702	0.698
0.4	0.626	0.660	0.683	0.694	0.695
0.5	0.625	0.634	0.642	0.685	0.687

(g) Temporal R with NDVI					
Slope / σ(VOD)	-20	-40	-80	-160	-320
0.025	0.599	0.607	0.563	0.403	0.222
0.05	0.590	0.613	0.585	0.445	0.320
0.1	0.587	0.646	0.637	0.517	0.426
0.2	0.612	0.662	0.678	0.661	0.629
0.3	0.620	0.655	0.669	0.667	0.655
0.4	0.620	0.646	0.658	0.659	0.653
0.5	0.602	0.610	0.616	0.651	0.647

480 **Fig. 4.** Second step of calibration: spatial correlation (R^2) between IB X-VOD and Bouvet AGB
481 (a), Saatchi AGB (b), CCI AGB (c), LAI (d) and NDVI (e) and temporal correlation (R)
482 between IB X-VOD and LAI (f), NDVI (g) for different values of (σ(VOD), slope). Red >
483 Orange > Yellow > light green > green > dark green represents the code of colours from the
484 highest R values to the lowest R values.

485 **3.1.3 Iterative calibration**

486 During the previous two steps, ω, H_R and VOD^{ini}, σ(VOD) were calibrated separately. We
487 performed an iterative analysis to finalize the calibration of these values. Thus, we re-run the
488 first step using the values of (slope, σ(VOD)) obtained in the second step (Fig. 5). To do so,
489 and to simplify the analysis, we only considered the parameter ω, as the parameter H_R had a
490 low impact on the results.

491 Taken together, it can be seen that ω = 0.06 is the optimum ω value in terms of spatial
492 correlation and very close to the optimum value in terms of temporal correlations. Therefore,
493 the iterative process confirmed the selected values obtained in the 1st and 2nd steps were optimal
494 values (ω = 0.06, H_R = 0.6, slope = -40 and σ(VOD) = 0.1).

ω	(a) Spatial R^2 with					(b)Temporal R with	
	Bouvet AGB	Saatchi AGB	CCI AGB	LAI	NDVI	LAI	NDVI
0.05	0.801	0.738	0.810	0.878	0.900	0.602	0.650
0.06	0.814	0.757	0.825	0.885	0.899	0.601	0.646
0.07	0.818	0.754	0.823	0.881	0.894	0.568	0.629

495

496 **Fig. 5.** Spatial and temporal correlation from the iterative step.

497 **3.2 IB X-VOD evaluation**

498 In order to evaluate the IB X-VOD product built in this study based on a calibration for year
499 2016, we considered a 3-year period (from year 2014 to 2016). This section will analyse the IB
500 X-VOD product from a spatial and temporal perspective.

501 **3.2.1 Spatial analysis**

502 Fig.6a illustrates the spatial distribution of the yearly average IB X-VOD. In general, X-VOD
503 ranged from 0 to 1.1. It can be seen that high VOD values were mainly distributed around the
504 equator (Congo and Gabon forests) with mean values close to 1.0. X-VOD gradually fell down
505 from the equator to higher latitudes both in northern and southern hemispheres. In the northern
506 hemisphere, X-VOD reduced to 0.6 at 10°N then plummeted to 0 in the Sahara Desert. In
507 comparison, X-VOD in the southern hemisphere showed a slower reduction tendency. X-VOD
508 dropped to approximately 0.8 between 5°S and 15°S, and continuously decreased to about 0.4
509 at 20°S, finally to even less than 0.2 along the southwest coastline of Africa. In Madagascar,
510 X-VOD was approximately 0.5 except over areas along the east coastline with values close to

0.8. The spatial patterns of IB X-VOD correspond well to those of Bouvet AGB (Fig.6b), Saatchi AGB (Fig.6c), CCI AGB (Fig.6d), LAI (Fig.6e), NDVI (Fig.6f) and high values (red colour) were found mainly in dense forests while low values were distributed in sparse vegetation and barren.

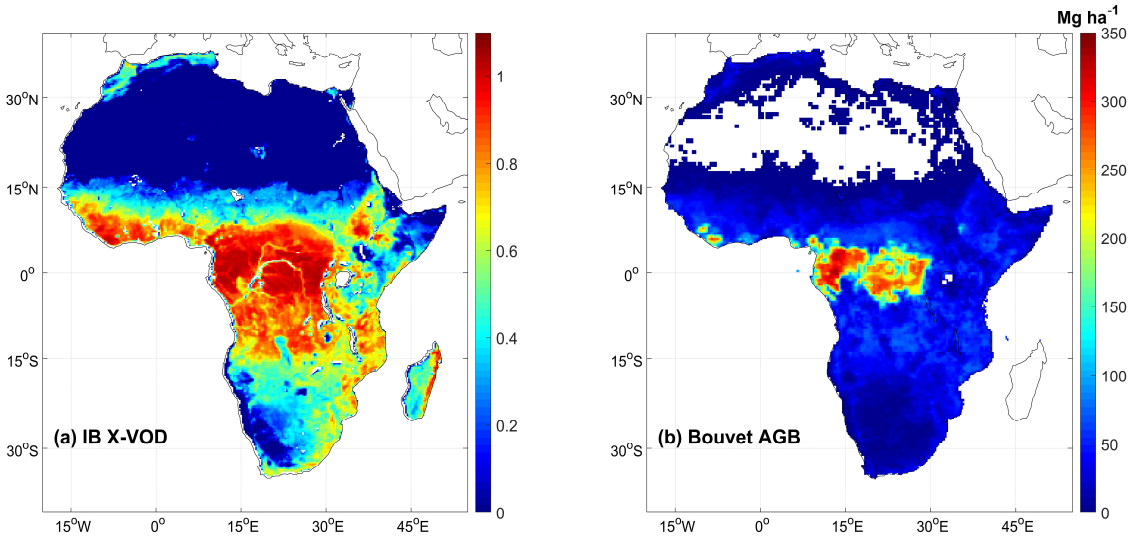

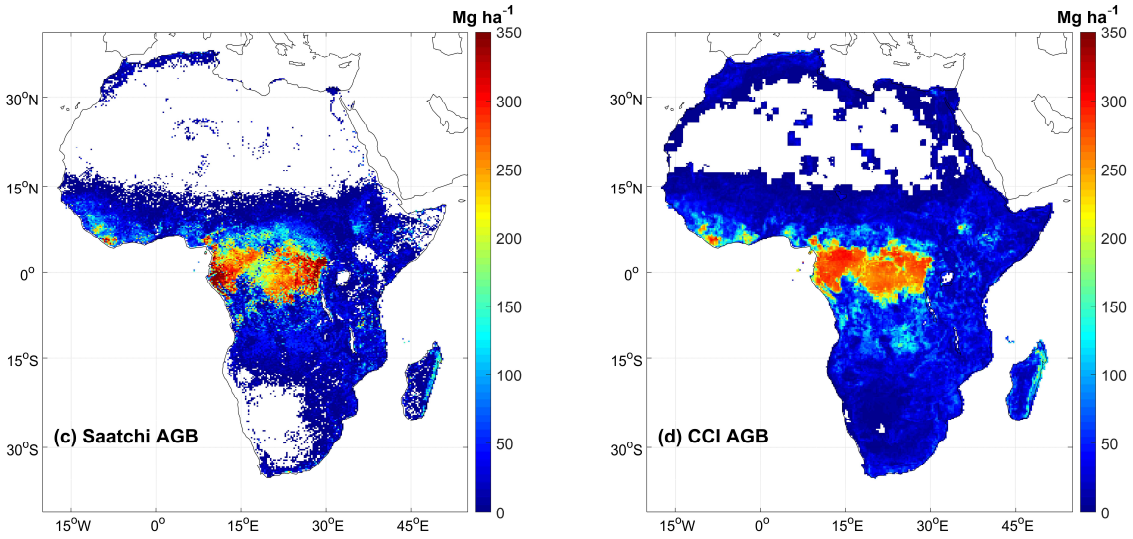

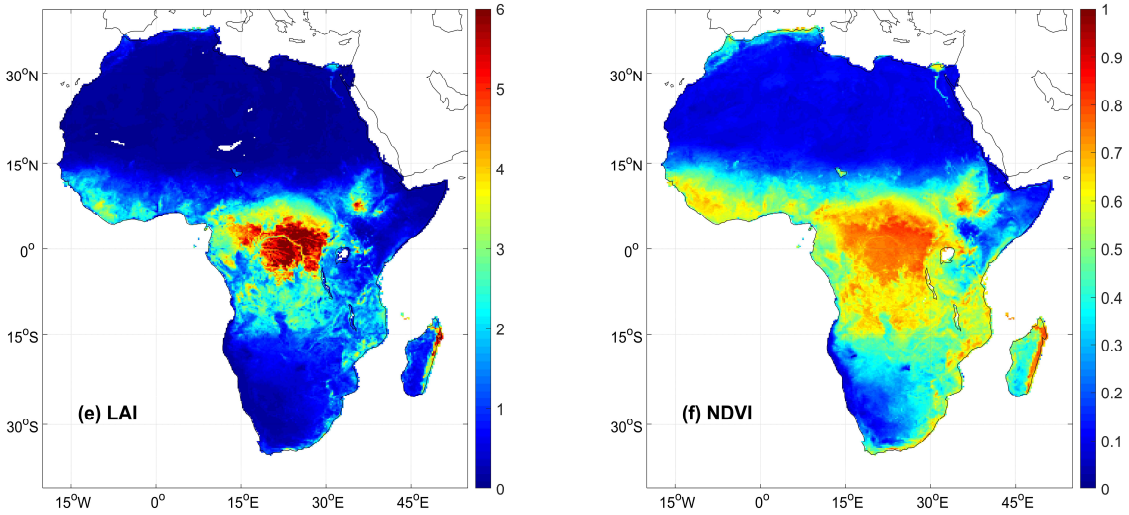

517

518 **Fig. 6.** Map of (a) IB X-VOD, (b) Bouvet AGB, (c) Saatchi AGB, CCI AGB (d), (e) LAI, (f)
519 NDVI.

520 Considering the IB X-VOD values for each IGBP class (Fig. 7a), we found that the highest X-
521 VOD values correspond to EBF (mean value of 0.93), then followed by MF, WSA (X-VOD >
522 0.8). DBF, SVA, CVM, CSH, CRO and GRA correspond to moderate X-VOD values (0.4 to
523 0.8 range). Lower X-VOD values were obtained in OSH and BAR (X-VOD < 0.4). Considering
524 all IGBP classes, a negative relationship was found between mean X-VOD and mean standard
525 deviation of VOD (Fig. 7b), except BAR which had low mean value and low standard deviation.
526 This result indicates the X-VOD values are more consistent for classes corresponding to dense
527 vegetation, while X-VOD is more variable for classes corresponding to sparser vegetation.

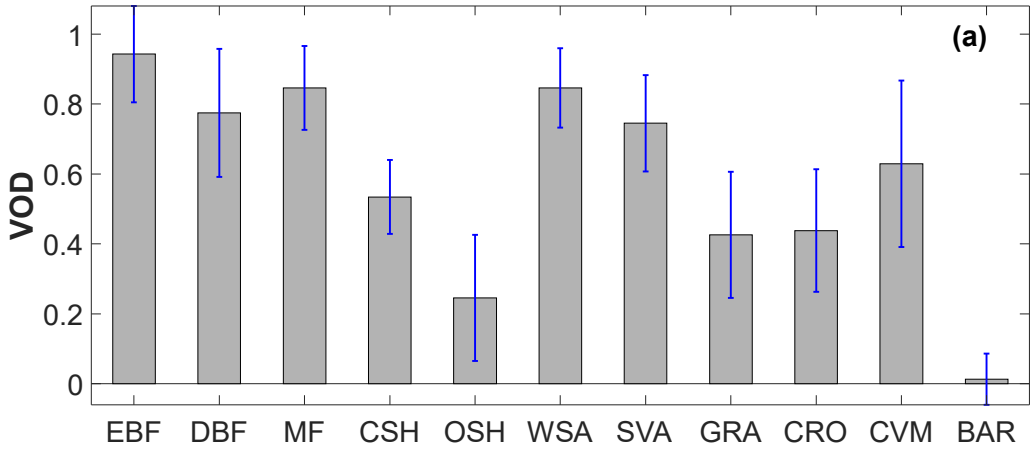

528

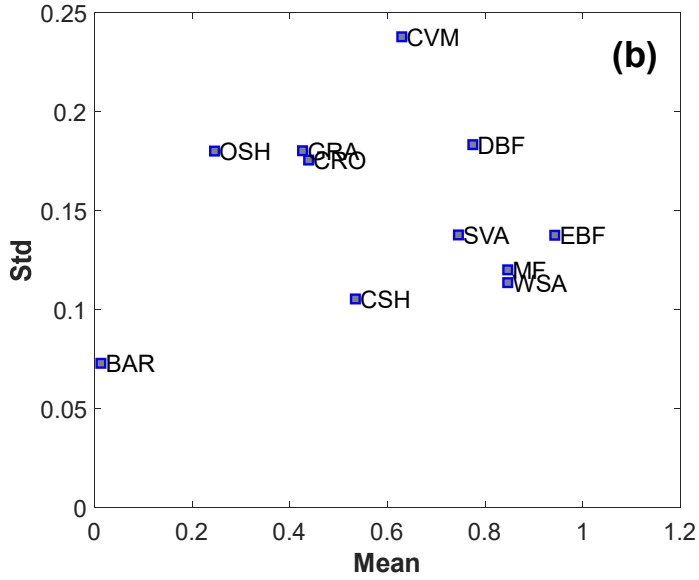

529

530 **Fig. 7.** (a) Mean IB X-VOD for each IGBP class (error bars represent the standard deviation
531 (std)); (b) Scatter plot of mean X-VOD vs standard deviation of X-VOD for each IGBP class.
532 We only retained IGBP classes which included more than 30 pixels.

533 **3.2.2 Temporal analysis**

534 This section mainly focuses on the performance of the temporal variations in IB X-VOD. In
535 general, X-VOD presents strong temporal correlation with LAI and NDVI especially for low
536 vegetation (Fig. 8). In the African continent, the correlation regularly increased from the equator
537 to higher latitudes both in the northern and southern atmospheres. The correlation with LAI in

538 dense vegetation (between 10° N and 5° S) was relatively low (R ~ 0.2) because of small
539 seasonality of vegetation and cloud cover for optical indices around the equator. Then it
540 gradually increased to values of R > 0.6 at the north of 10° N and the south of 5° S. Angola
541 even produced a mean correlation of 0.9 in the red-coloured southern regions of the map. Higher
542 temporal correlations with X-VOD were obtained with NDVI than with LAI for all vegetation
543 classes, except over evergreen broadleaf forest (EBF), where lower correlation values were
544 obtained (R ~ 0.2) (Fig. 8c d).

545 More specifically, values of temporal correlation varied significantly among the different
546 vegetation types. Shrublands (OSH and CSH) produced very high correlations (R ~ 0.9),
547 followed by DBF, MF, GRA, SVA, CRO and WSA with correlations all exceeding 0.57. The
548 remaining two classes (EBF and CVM) had low correlation. Mean temporal correlation (for
549 both relationships VOD / LAI and VOD / NDVI) generally decreased with increasing mean
550 VOD values (Fig. 8d).

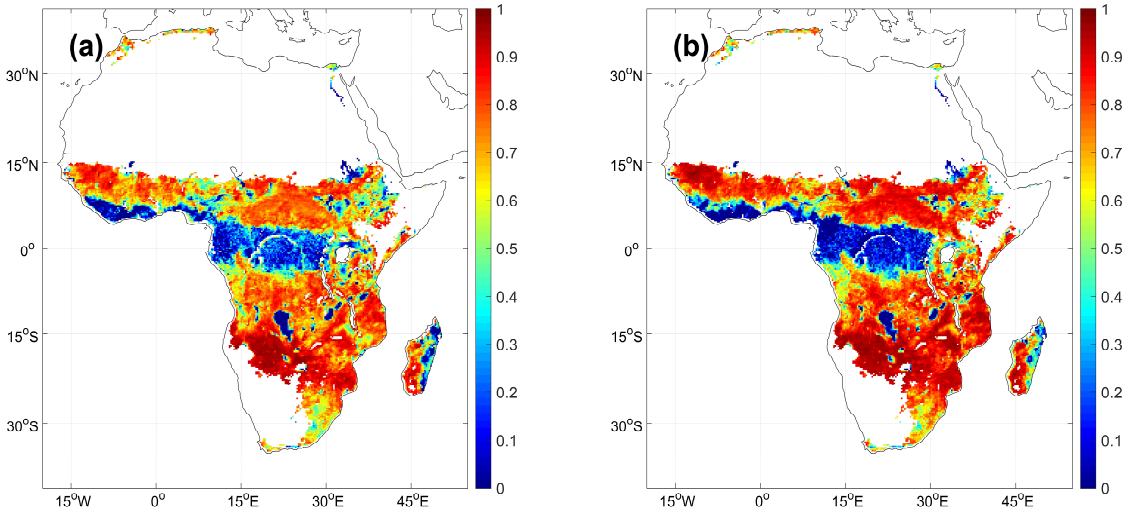

551

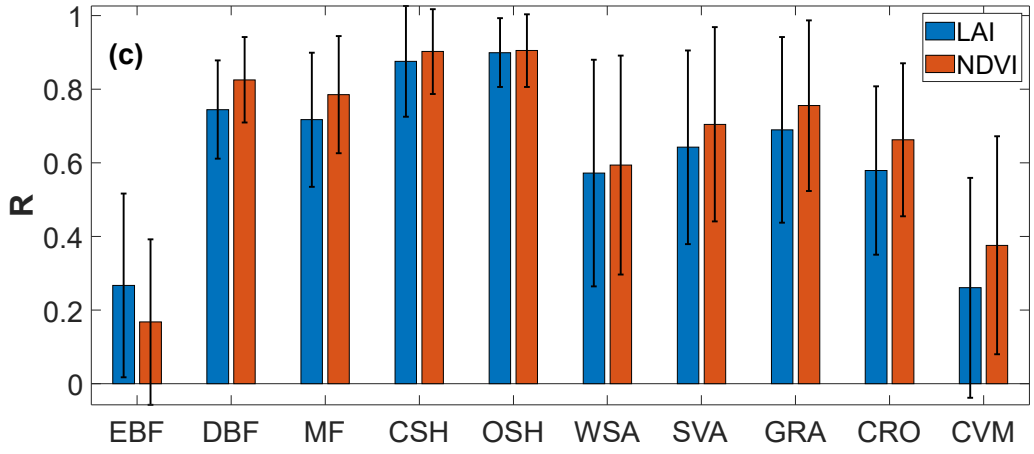

552

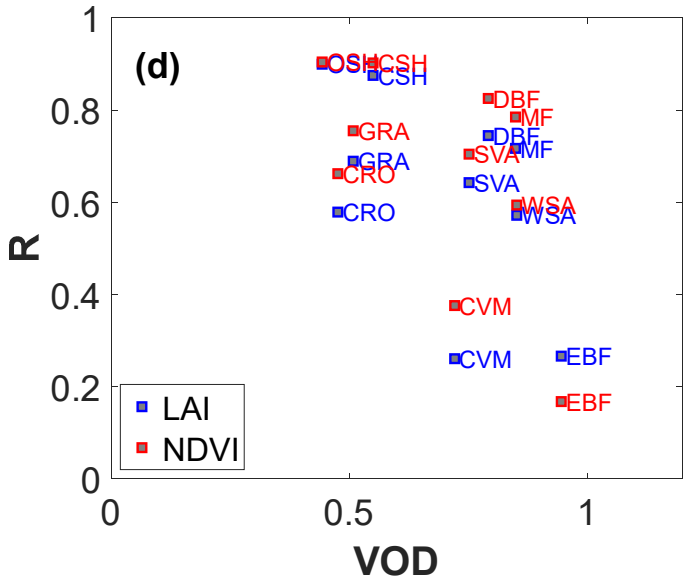

553

554 **Fig. 8.** Map of the temporal correlation (R) between (a) IB X-VOD and LAI and (b) IB X-VOD
555 and NDVI; (c) Histogram of R values for each IGBP class; (d) Scatter plot between R and mean
556 VOD values for each IGBP class. We only retained IGBP classes which included more than 30
557 pixels.

558 **3.3 Comparison with other X-VOD products**

559 Due to the lack of reference values from in-situ measurements or models, it is a big challenge
560 to validate the VOD products, especially at a continental scale (Li et al., 2021). In this section,
561 the performance of IB X-VOD was assessed through an inter-comparison with three other X-

562 VOD products (LPDR, VODCA and LPRM). The metrics considered here were spatial
563 correlation computed between X-VOD and the Bouvet AGB, Saatchi AGB, CCI AGB, LAI
564 and NDVI and the temporal correlation with LAI and NDVI.

565 Note that the same metrics were used for calibration (section 3.1) and for evaluation (this
566 section): this may be considered as circular. Let us explain better our approach: our objective
567 in developing IB X-VOD was to develop a new X-VOD product producing good scores in terms
568 of spatial and temporal correlation. To evaluate if we reached our goal, we compared the scores
569 obtained with our new product (IB-X-VOD) and other X-VOD products. There is circularity,
570 but circularity was intentional in our approach. The obtained score should be the main criteria
571 of choice for users interested in applications, no matter what calibration approach was used.
572 Moreover, circularity was limited by considering only one year for calibration (2016) and three
573 years (2014-2016) for validation.

574 **3.3.1 Spatial performances**

575 Fig. 9 presents spatial scatter plots between mean X-VOD and the mean values of four
576 vegetation parameters (Bouvet AGB, Saatchi AGB, CCI AGB, LAI, NDVI; average values
577 computed over 2014 to 2016). It can be seen that AGB and LAI are almost exponentially related
578 with X-VOD, while NDVI presents a relatively good linearity with X-VOD. In comparison
579 with other products, IB X-VOD produced higher R^2 values of 0.82, 0.76, 0.83 and 0.94
580 respectively with Bouvet AGB, Saatchi AGB, CCI AGB and NDVI. Even though X-MEB
581 obtained a lower score with LAI, the value ($R^2 = 0.88$) obtained by IB X-VOD is very close to
582 the best one ($R^2 = 0.89$) obtained by LPRM. It seems that LPDR VOD is not prone to saturate
583 in dense vegetation, but it is slightly more scattered, especially when LPDR X-VOD exceeds
584 2.0 (second column in Fig. 9). Note that LPDR shows a higher VOD range (0-3) than the other
585 products. The main reason is that LPDR regards the soil as dry bare soil. Consequently, LPDR
586 X-VOD does not include only vegetation effects but also surface roughness effects, possibly

leading to this high range of VOD values. However, as there is a lack of reference values from in-situ measurements to define the absolute range of VOD, scientists only focus on the relative variations of VOD and the inter-comparison of the absolute values of the VOD ranges is rarely considered as meaningful.

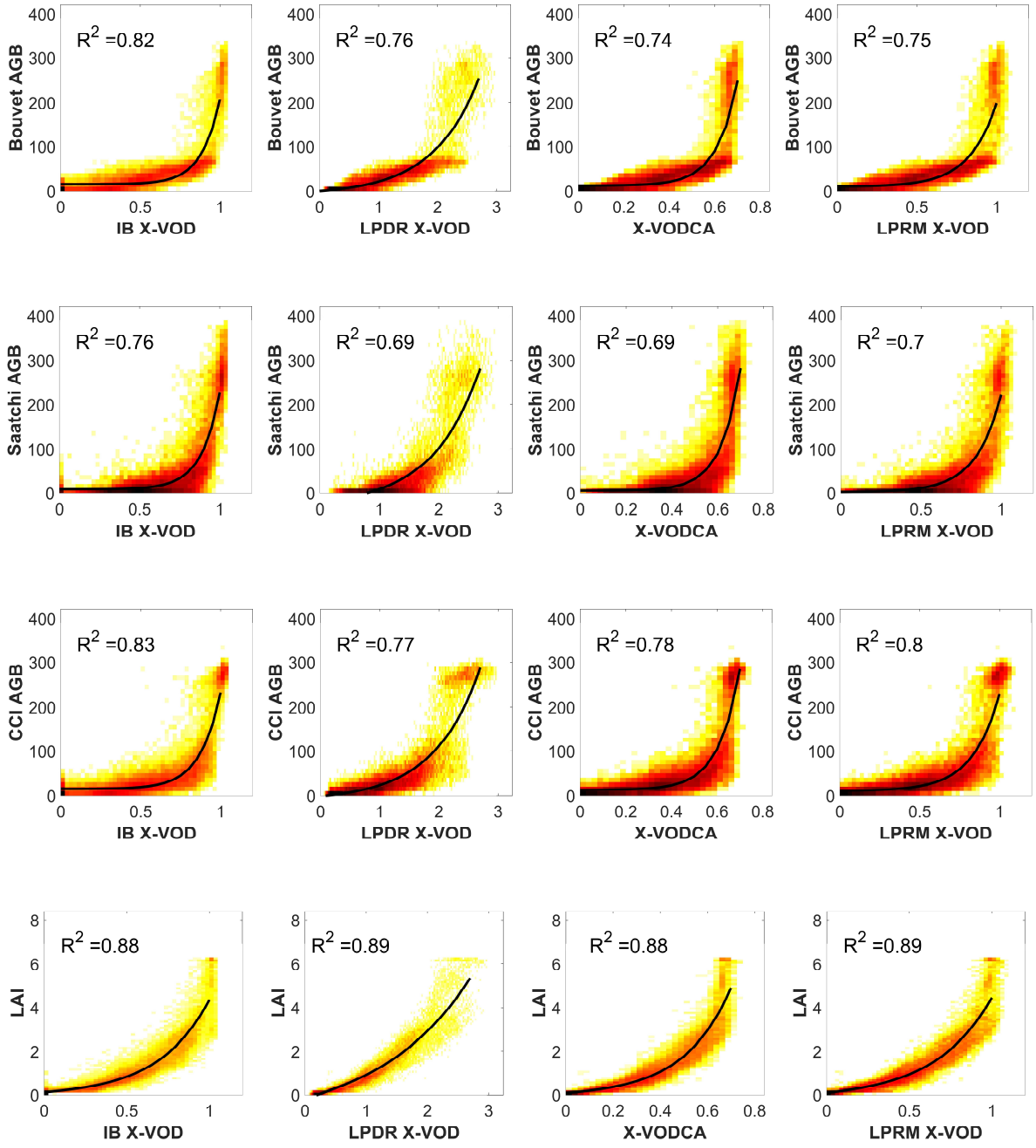

595 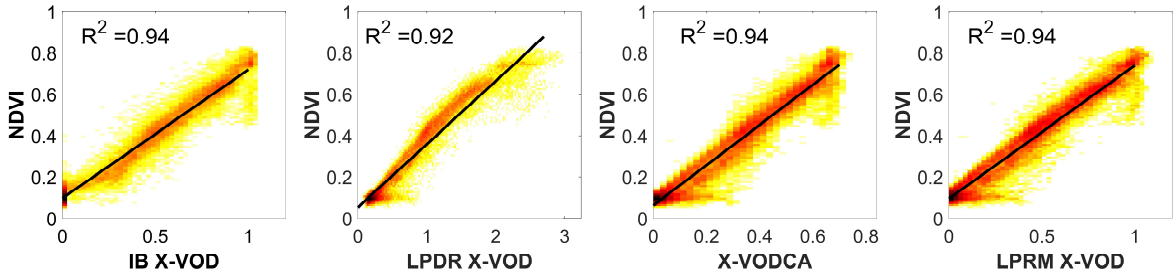

596 **Fig. 9.** Density scatter plot between average IB X-VOD (1st column), LPDR X-VOD (2nd
597 column), VODCA X-VOD (3rd column), LPRM X-VOD (4th column) and Bouvet AGB (1st
598 row), Saatchi AGB (2nd row), CCI AGB (3rd row), LAI (4th row), NDVI (5th row) (numbers
599 were rounded to 2 digits).

600

601 **3.3.2 Temporal performances**

602 Similar to the inter-comparison done in terms of spatial correlation in the previous section, an
603 inter-comparison was achieved in terms of temporal correlation. Generally, IB X-VOD
604 obtained very good scores considering LAI in Africa, especially over the centre-west (from
605 approximately 15° S to 7° N and from the western coastline to 30° E, orange pixels). LPDR X-
606 VOD obtained good scores mainly in the east of Africa and Madagascar (green pixels). Best
607 scores for VODCA X-VOD were mainly located near 10° N latitude (light blue) and those for
608 LPRM X-VOD were scattered all over Africa (dark blue) (Fig. 10a). The performance of the
609 four X-VODs varied for different vegetation classes (Fig. 10c). IB X-VOD obtained best scores
610 in EBF, DBF, MF, CSH, OSH, WSA and SVA (best scores over at least 60% of pixels for each
611 vegetation class). For GRA, CRO and CVM, classes corresponding to relatively low vegetation
612 canopies, scores of LPDR X-VOD surpassed the others. Considering NDVI instead of LAI, the
613 spatial patterns and the distribution of scores amongst the different classes for the different X-
614 VOD products is almost the same (Fig. 10bd).

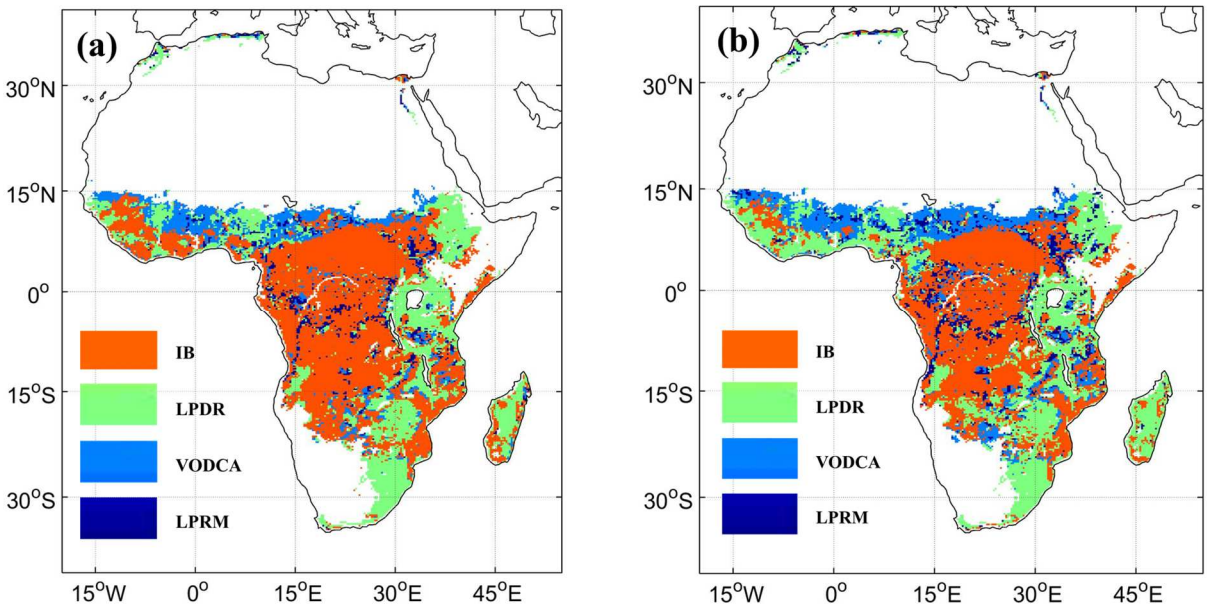
(a)
(b)
30°N
15°N
0°
15°S
30°S
15°W
0°
15°E
30°E
45°E
IB
LPDR
VODCA
LPRM

615

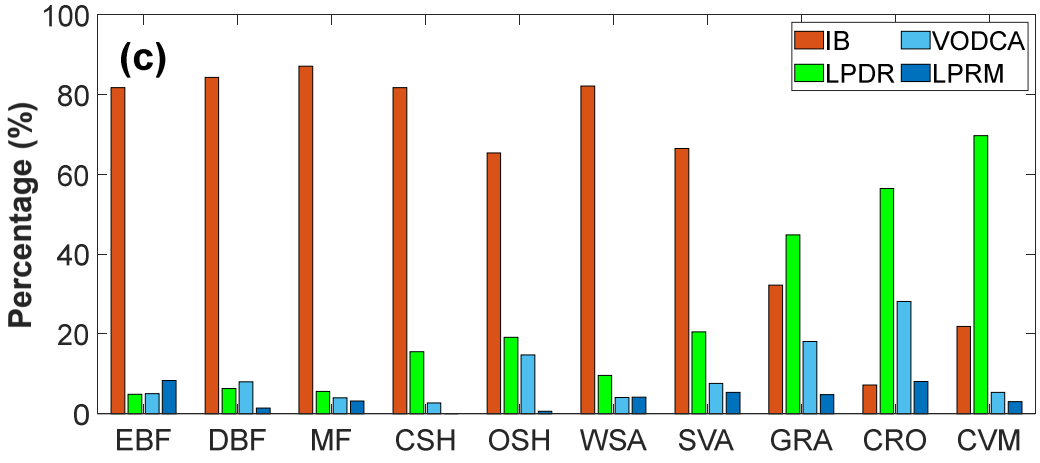
(c)
Percentage (%)
100
80
60
40
20
0
IB
VODCA
LPDR
LPRM
EBF
DBF
MF
CSH
OSH
WSA
SVA
GRA
CRO
CVM

616

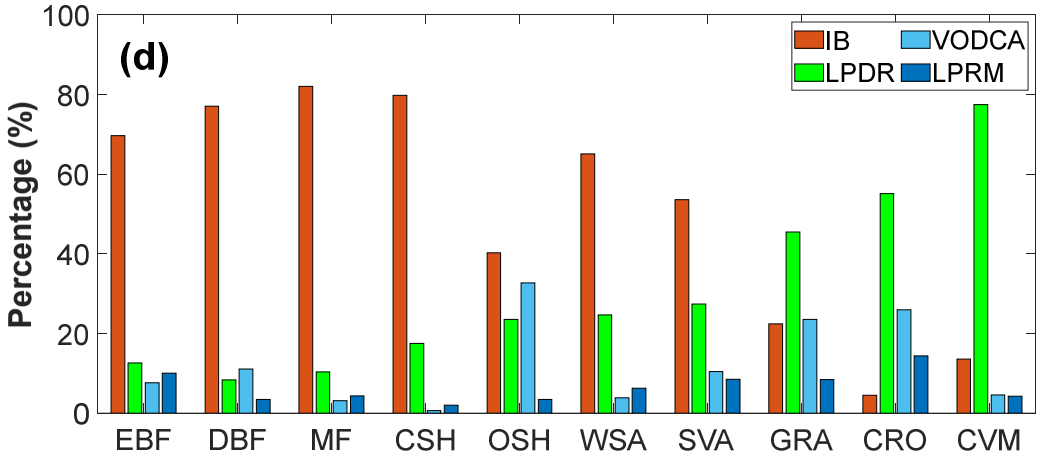
(d)
Percentage (%)
100
80
60
40
20
0
IB
VODCA
LPDR
LPRM
EBF
DBF
MF
CSH
OSH
WSA
SVA
GRA
CRO
CVM

617

Fig. 10. Spatial distribution showing which X-VOD product (IB, LPDR, VODCA, LPRM) produced the highest temporal correlation with (a) LAI or (b) NDVI; (b) Performances of the four X-VOD products for each vegetation class with (c) LAI or (d) NDVI.

Fig. 11 summarizes the overall performance of the four different X-VOD products in terms of temporal correlation with LAI and NDVI. Average values of temporal correlations with LAI in Africa exceed 0.5 for the four products with IB X-VOD presenting highest correlation ($R \sim 0.6$). In comparison with the relationships with LAI, correlation with NDVI was found to be stronger ($R > 0.6$ for all X-VOD products). More specifically, the advantage of IB X-VOD was more obvious in dense forests (EBF): the temporal correlation with LAI or NDVI reached 0.27 in EBF, while other products showed a relatively poor performance with very low or even negative correlations (Fig. 11a). The potential reason could be the use of modelled SM from ERA5-Land in computing IB X-VOD. It is well known that it is hard to accurately estimate SM in densely vegetated areas from microwave observations since the signal emitted from the soil is significantly attenuated by vegetation, particularly at X-band; while the errors of model simulations are not significantly affected by the dense vegetation. Thus, the ERA5-Land dataset may provide a more reliable SM input in dense forests than that obtained from remote sensing observations.

Based on the statistics of dominant products producing the highest temporal correlation with LAI or NDVI for each pixel in Africa (Fig. 11b), we found that best scores were generally obtained for IB X-VOD (over 54% of the pixels in Africa *vs* 29%, 12% and 6% of the pixels, for, respectively, the LPDR, VODCA and LPRM algorithms). Similar results were obtained considering NDVI instead of LAI, but the score of IB decreased to the advantage of all the three other products (43%, 33%, 20%, 10% of the pixels for, respectively, the IB, LPDR, VODCA and LPRM algorithms). One of the reasons explaining the good results of IB X-VOD could be

that the modelled temperature datasets from ERA5 Land rather than TB-based temperature estimates were used in this study. Evaluation studies found model temperature simulations are more accurate than the temperature estimated by TB, such as the temperature proxy used in the LPRM model (Cui et al., 2018; Ma et al., 2019) and the latter shows large uncertainty in some regions, such as the Tibetan Plateau (Zeng et al., 2015). Another reason is that a priori information (constraints) was used in the X-MEB model inversion. In comparison to the use of a very weak constraint to the initial VOD during the first calibration step (σ(VOD) = 0.5), we found the VOD retrieval was improved after we used a strong constraint in the second calibration step (σ(VOD) = 0.1).

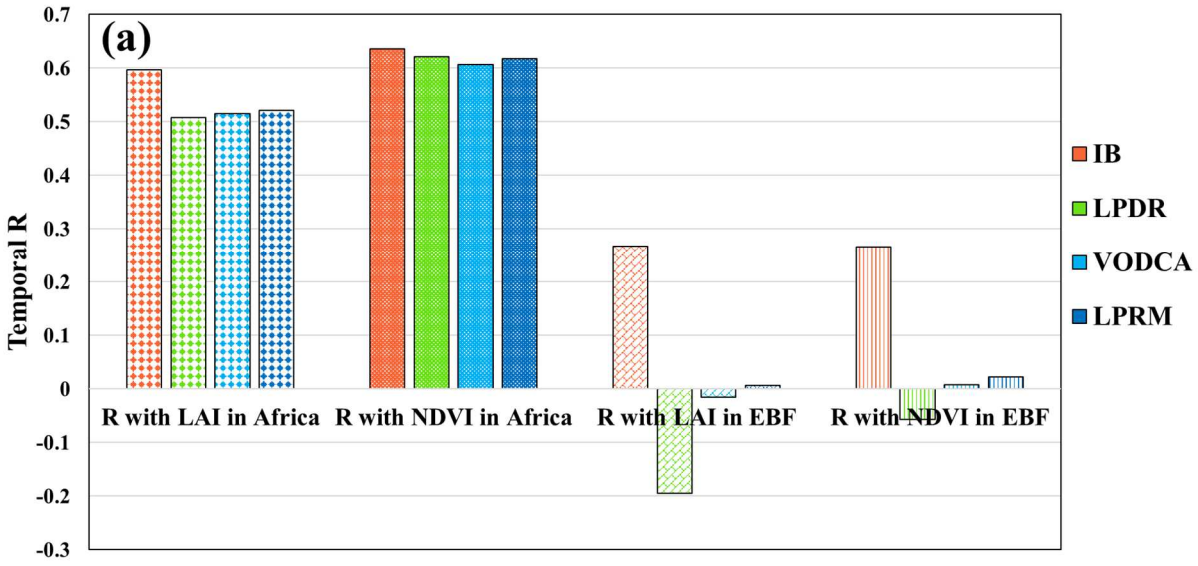

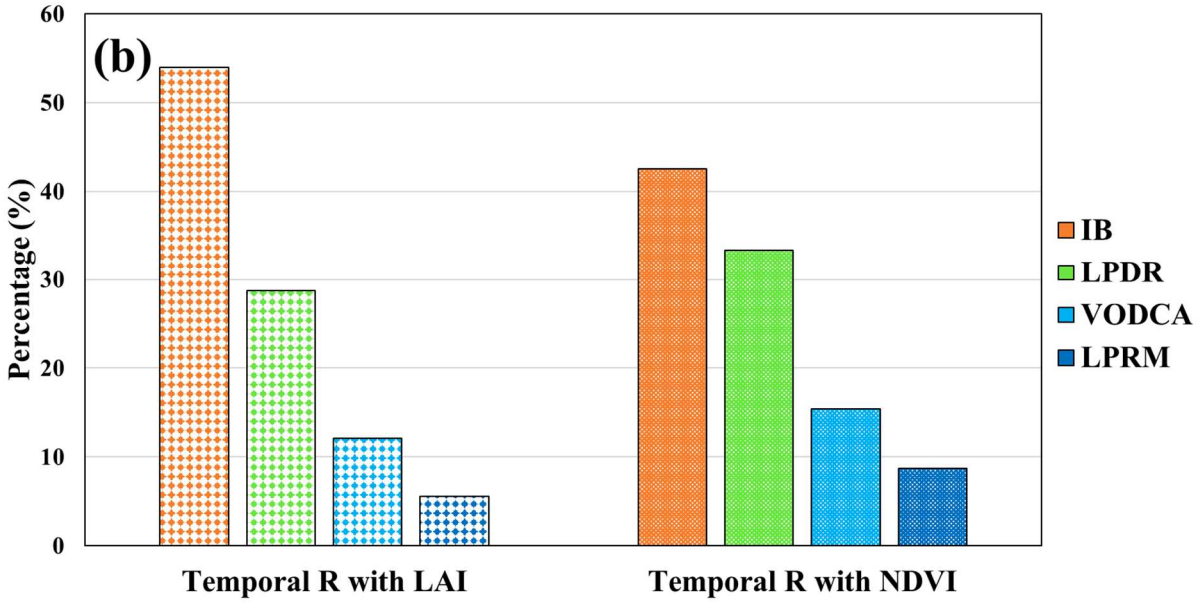

Fig. 11. (a) Average values of temporal correlation (R) with LAI or NDVI in the whole Africa or in EBF; (b) Temporal performance of the four X-VOD products in Africa showing the percentage of pixels where best temporal correlation was obtained.

Discussion

In this study, the vegetation extinction parameter (VOD) is retrieved from passive microwave observations using a radiative transfer equation which also considers another important parameter, soil moisture (Njoku et al., 1977; Paloscia et al., 2001; Mladenova et al., 2014; Pan et al., 2014; Paloscia et al., 2006). Soil moisture presents high spatial variability in space and time, due to the heterogeneity of the land surface and the variability of precipitation (Owe et al., 2001). In this study, we focused exclusively on the retrieval of VOD, and ERA5-Land SM was selected as a known input of the retrieval algorithm in consideration of its high accuracy, high frequency and long-time series of records. Therefore, the X-VOD retrievals made in this study may be sensitive to the quality of the ERA5-Land SM dataset. Errors associated with the VOD retrievals and originating from the used SM estimate may include the following: i) modelling errors associated with the estimates of ERA5-Land SM (ubRMSE = 0.05 m3/m3,

669 Chen et al., 2021), ii) errors associated with calibrating the soil and vegetation parameters (ω
670 and H_R), iii) inconsistency in the top soil layer corresponding to the sampling depth of the
671 observations made at X-band and the simulations from ERA5-Land. For instance, the
672 microwave brightness temperature observations at X band are sensitive to the soil moisture in
673 the top ~ 1 cm of the soil (Owe et al., 2008), while top-layer ERA5-Land SM used in this study
674 corresponds to the 0-7 cm soil layer. This inconsistency was partially corrected for by the
675 calibration of the soil roughness effects which may account for differences in the absolute
676 values of SM in the 0-7cm and the 0-1cm top soil layers. However, for an optimal correction,
677 a temporally-dynamic roughness parameter (H_R) would be required. More generally, we
678 considered both ω and H_R were constant in time and space. The calibration results indicated
679 that the VOD retrievals were more sensitive to ω than to H_R (Fig. 3). The calibrated value of ω
680 (= 0.06) in this study agreed well with that of the LPDR and LPRM algorithms (Du et al., 2015;
681 Owe et al., 2001). However, previous studies suggested the effective vegetation scattering
682 albedo varies seasonally and depends on vegetation types (Kurum, 2013; Wigneron et al., 2004;
683 Feldman et al., 2018; Baur et al., 2019). For instance, Konings et al. (2016) retrieved a map of
684 ω showing higher values in areas covered by significant woody components, such as forests
685 and woody savannas, and lower values in less densely vegetated areas. Konings et al. noted too
686 that there was noticeable variability in the values of ω because of the mixed plant species or
687 different phenology conditions. In addition, some studies found the effective scattering albedo
688 varies for the V- and H-polarizations especially at large incidence angles, such as 55° for
689 AMSR2 (Zhao et al., 2020; Van de Griend et al., 1996). Wang et al. (2015), Fernandez-Moran
690 et al. (2017) and Karthikeyan et al. (2019) suggested a similar trend for H_R: higher values for
691 dense vegetation and lower values for sparse vegetation. In consideration of these studies,
692 IGBP-based or pixel-based and polarization-dependent values of ω and H_R should be evaluated
693 in future works. However, the fact that our calibration of ω and H_R is not dependent on any

694 vegetation classification is an advantage, as it limits the use of ancillary data in the algorithm
695 and makes the product more robust *vs* circularity (Wigneron et al., 2021).

696 The calibration step was conducted using spatial and temporal correlation as criteria. However,
697 Fig. 3 to 6 indicated that the parameter groups which produced highest spatial correlation are
698 not quite consistent with those producing highest temporal correlation. In this study, we gave
699 priority to spatial correlation. Therefore, we only set a minimum threshold value ($R > 0.6$) for
700 temporal correlation; if the latter condition was satisfied we focused on spatial correlation.
701 Finding a good way to consider both spatial and temporal correlations would be a priority in
702 future studies.

703 The temporal evaluation of IB X-VOD against LAI and NDVI shows that very high correlations
704 were obtained for low vegetation, especially for Shrublands (OSH and CSH) and vegetation
705 covers with a high seasonal variability (DBF, MF, GRA). On the contrary, low correlation was
706 obtained for EBF. This may result from i) the small seasonal variability of vegetation over dense
707 canopies which makes it difficult to capture a strong relationship between X-VOD and LAI or
708 NDVI. It may also be related to ii) the atmospheric effects and cloud cover that affect the
709 accuracy of the optical indices and consequently decrease the correlation values with X-VOD.
710 In addition, iii) the changes in vegetation greenness measured by the optical vegetation indices
711 (NDVI and LAI) are not always in phase with those of the vegetation features (VOD, AGB,
712 water content) measured from the microwave sensors. For example, the changes of greenness
713 measured in the optical domain over the Amazon forest resulted from an artefact of the
714 variations in the sun-sensor geometry that affected the near-infrared reflectance (Morton et al.,
715 2014). Similarly, a large time lag may exist between the vegetation greenness estimated from
716 optical sensors and the vegetation water content as retrieved from the microwave sensors,
717 particularly in the tropics (Jones et al., 2014, Tian et al., 2018).

In general, IB X-VOD obtained better scores than the other X-VOD products in terms of temporal correlation with LAI and NDVI. However, for some low vegetation types (GRA, CRO and CVM) (Fig. 12a), LPDR X-VOD overperformed IB X-VOD. A possible reason is that daily LPDR X-VOD was smoothed using a 30-day moving median filter (Jones et al., 2011; Du et al., 2015). This filtering step may help improving the temporal continuity in the X-VOD time series and reduce short-term noises. In producing IB X-VOD, we did not use a moving filter to smooth the time series considering that it may also eliminate real features of the vegetation dynamics (Feldman et al., 2020). Over some other pixels (Fig. 12b), IB X-VOD obtained a better score with LAI, but not for NDVI. The LAI algorithm applied climatology temporal smoothing and gap filling techniques to ensure consistency and continuity as well as short-term projection of the product dynamics (Verger et al., 2014). Thus, the filtering of the high frequency changes in the vegetation signal made in both LAI and LPDR X-VOD may have affected the results of the evaluation made here. Moreover, there are also time lags between VOD and optical vegetation indices (for instance a ~40-day time lag between VOD and LAI agreeing with the study of Tian et al., (2018) could be noted in Fig. 12ab) which may affect too our evaluation results and should be investigated further in future studies.

Microwave remote sensing shows competitive performances in many fields (such as monitoring vegetation water status, biomass, etc.) in comparison to the optical domain (Morton et al., 2014; Konings et al., 2017b). However, the primary limitation of X-VOD lies in its coarse spatial resolution (25 km) which makes it more suitable for applications at continental and global scales. Spatial resolution enhancement of VOD is a necessity in order to provide detailed information on vegetation at local and field scales, such as for the study of agricultural crops under different natural and man-made environments. Therefore, a key step in improving the IB X-VOD product will be to evaluate downscaling methods as proposed in the literature (Santi, 2010; Sabaghy et al., 2020; Gevaert et al., 2016; Abowarda et al., 2021; Gao et al., 2020). In addition, fine-spatial-

743 resolution datasets for soil moisture and temperature will be needed to run the X-MEB model.
744 Many high-resolution soil moisture and temperature products, such as published in Long et al.
745 (2019, 2020) and Peng et al. (2020) could be used as potential input datasets.

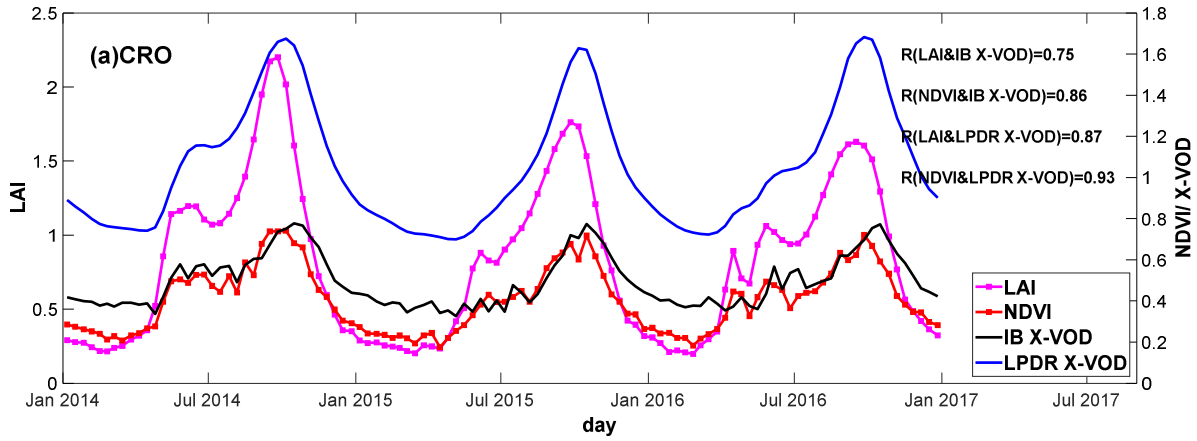

746

747

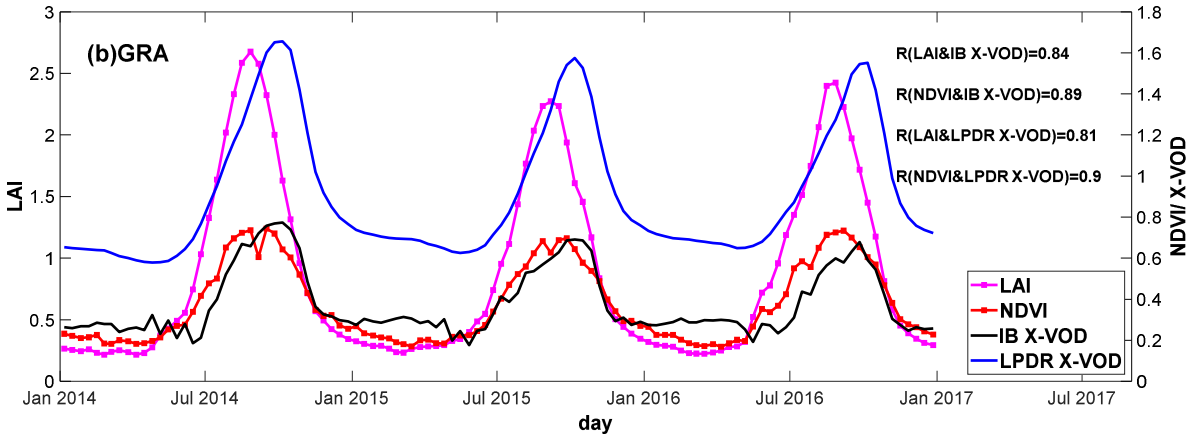

748

749 **Fig. 12.** Time series of LAI (magenta), NDVI (red), IB X-VOD (black) and LPDR X-VOD
750 (blue) for one pixel over crops (CRO) (a) and one grasslands (GRA) pixel (b) from 2014 (1st
751 Jan) to 2016 (31st Dec) (numbers were rounded to 2 digits).

Conclusion and perspectives

The general aim of the present study was to evaluate a new approach for computing X-VOD from the dual-channel X-band passive microwave observations of AMSR2. Thus, in this evaluation step, IB X-VOD was computed only over Africa during 2014-2016. Globally-constant values (ω = 0.06 and H_R = 0.6) were found to achieve high spatial and temporal correlations with the reference vegetation parameters (Bouvet/ Saatchi/ CCI AGB, LAI and NDVI). Comparison with other X-VOD products suggested IB X-VOD had competitive advantages in terms of both spatial and temporal performances. In particular, spatial correlation with three biomass datasets (R^2 ~ 0.76-0.83) was found to be higher with IB X-VOD than for the other X-VOD products and temporal correlation with LAI or NDVI, particularly for dense tropical forests, showed obvious improvement.

In consideration of the good general performance of this new X-VOD product, future activities will consider, in a first step, to extend the production of IB X-VOD to the global scale and to the whole observation period of AMSR2 (2012-present). RFI effect needs to be considered during this spatial extension especially in Europe where RFI at X-band cannot be ignored (Nijs et al., 2015; Lacava et al., 2012; Njoku et al., 2005). In a second step, we will consider extending the production (i) to AMSR-E to build a long-term (AMSR-E/ AMSR2) data set, (ii) to dual polarizations at the X-band and (iii) to the C-band. When building the AMSR-E/ AMSR2 X-VOD time series a great attention will be given to the merging method to avoid time discontinuities as revealed for other merged products (Li et al., 2020, 2021). To incorporate both the H and V polarizations in the cost function, the polarization mixing effects need to be considered as suggested in the literature (Shi et al., 2005; Njoku and Chan, 2006; Lawrence et al., 2013; Peng et al., 2017). In a third step, spatial resolution enhancement will be conducted

776 to provide detailed VOD information at local and field scales. Note that the specific approach
777 developed here to avoid the ill-posed issue of retrieving simultaneously VOD and SM from
778 dual channel observations can be extended to other passive (*e.g.* SMAP and SMOS) or active
779 (*e.g.* ASCAT) microwave satellites.

780

781

Data availability

IB X-VOD was developed by INRAE (Institut national de recherche pour l'agriculture, l'alimentation et l'environnement). IB X-VOD will be made available at the INRAE Bordeaux remote sensing lab website (https://ib.remote-sensing.inrae.fr).

Author contribution

Jean-Pierre Wigneron and Mengjia WANG designed the algorithm. Mengjia Wang did the numerical experiments and wrote the first draft. J-P Wigneron helped to improve the manuscript. All authors contributed to the discussion and revised the submitted manuscript.

Competing interests

The authors declare that they have no conflict of interest.

Acknowledgements

This work was supported by CNES-TOSCA (Centre National d'Etudes Spatiales, France) funding and Mengjia WANG was sponsored by China Scholarship Council (CSC; 201906040124). Lei Fan acknowledges additional support from the National Natural Science Foundation of China (Grant no. 41801247) and Natural Science Foundation of Jiangsu Province (Grant no. BK20180806). We wish to thank the three reviewers for their helpful comments that strongly contributed to improve the manuscript.

Appendix table and figure

Appendix Table 1. MODIS Land Cover

Land Cover Type	Acronym
Evergreen Needleleaf Forests	ENF
Evergreen Broadleaf Forests	EBF
Deciduous Needleleaf Forests	DNF
Deciduous Broadleaf Forests	DBF
Mixed Forests	MF
Closed Shrublands	CSH
Open Shrublands	OSH
Woody Savannas	WSA
Savannas	SAV
Grasslands	GRA
Permanent Wetlands	WET
Croplands	CRO
Urban and Built-Up Lands	URB
Cropland/Natural Vegetation Mosaics	CVM
Snow and Ice	SNO
Barren	BAR
Water Bodies	WAT

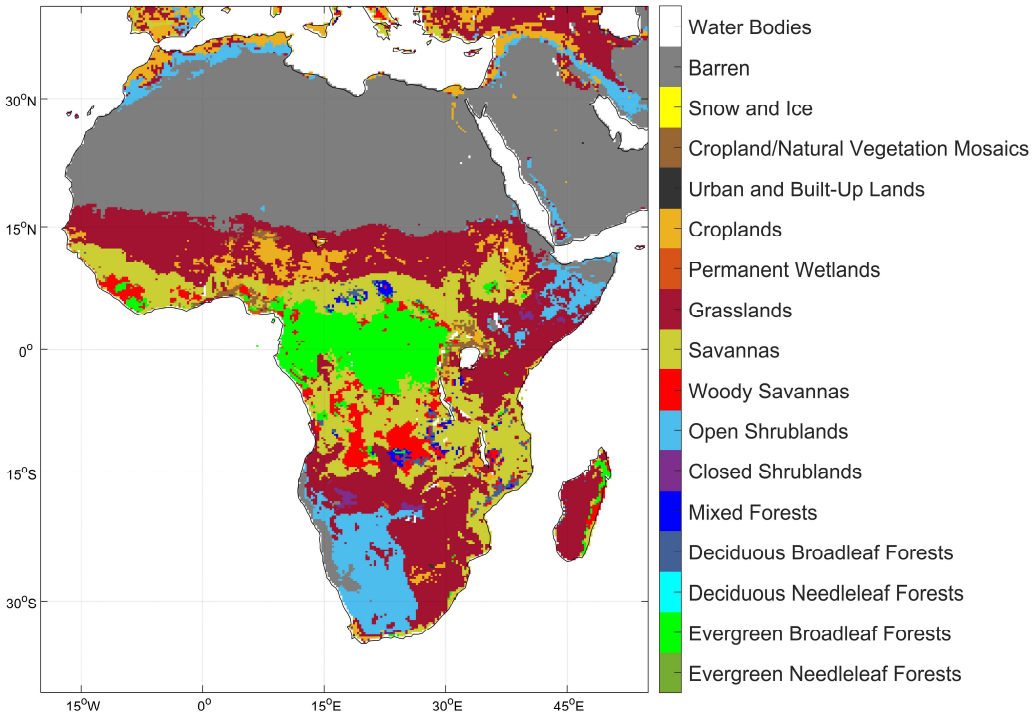

803

804 **Appendix Fig. 1.** Distribution of the IGBP vegetation classes in Africa

805

806 **Appendix Table 2.** Summary of datasets used in this study

Variable name	Producer/ Sensor	Sampling	Period	Function	References
Brightness temperature	AMSR2	Daily, 0.25°	1/2016 – 12/2016	Calibration	JAXA (2013)
			1/2014 – 12/2016	Evaluation	
Download link: https://suzaku.eorc.jaxa.jp/GCOM_W/data/data_w_index.html					
Soil moisture (0-7 cm under the surface)	ECMWF ERA5 Land	Hourly, 0.25°	1/2016 – 12/2016	Calibration	C3S (2019)
			1/2014 – 12/2016	Evaluation	
Skin temperature	ECMWF ERA5 Land	Hourly, 0.25°	1/2016 – 12/2016	Calibration, Vegetation canopy temperature	
			1/2014 – 12/2016	Evaluation, Vegetation canopy temperature	
Soil temperature (0-7 cm and 28-100 cm under the surface)	ECMWF ERA5 Land	Hourly, 0.25°	1/2016 – 12/2016	Calibration, Soil temperature	
			1/2014 – 12/2016	Evaluation, Soil temperature	
Download link: https://cds.climate.copernicus.eu/					
Saatchi AGB	Saatchi	1km	2015	Evaluation	Saatchi et al. (2011)
Bouvet-Mermoz AGB	Bouvet-Mermoz	25 m	2010	Evaluation	Bouvet et al. (2018) Mermoz et al. (2015)
CCI AGB	CCI	100 m	2017	Evaluation	Santoro et al. (2019)
Download link: http://data.ceda.ac.uk/neodc/esacci/biomass/data/agb/maps/2017/v1.0/					
LAI	CGLS	10-day, 1km	1/2014 – 12/2016	Evaluation	Buchhorn et al. (2017) Swinnen et al. (2017)
NDVI	CGLS	10-day, 1km	1/2014 – 12/2016	Evaluation	
Download link: https://land.copernicus.eu/global/					
LPDR X-VOD	University of Montana/ AMSR2	Daily, 25km	1/2014 – 12/2016	Inter-comparison	Du et al. (2015, 2017)
Download link: https://nsidc.org/data/					
LPRM X-VOD	Vrije Universiteit Amsterdam and NASA/ AMSR2	Daily, 0.25°	1/2014 – 12/2016	Inter-comparison	Owe et al. (2001, 2005, 2008)
Download link: https://disc.gsfc.nasa.gov/datasets/					

VODCA X-VOD	Technische Universität Wien/ AMSR2	Daily, 0.25°	1/2014 – 12/2016	Inter-comparison	Moesinger et al. (2020)
Download link: https://zenodo.org/record/2575599					
Land cover	MODIS	Yearly, 500m	2015	Analysis	Friedl & Sulla-Menashe (2019)
Download link: https://modis.gsfc.nasa.gov/data/dataprod/mod12.php					

807

References

Abbott, B. W., Bishop, K., Zarnetske, J. P., Minaudo, C., Chapin, F. S., Krause, S., ... & Plont, S. (2019). Human domination of the global water cycle absent from depictions and perceptions. Nature Geoscience, 12(7), 533-540.

Abowarda, A. S., Bai, L., Zhang, C., Long, D., Li, X., Huang, Q., & Sun, Z. (2021). Generating surface soil moisture at 30 m spatial resolution using both data fusion and machine learning toward better water resources management at the field scale. Remote Sensing of Environment, 255, 112301. doi: 10.1016/j.rse.2021.112301

Baret, F., Hagolle, O., Geiger, B., Bicheron, P., Miras, B., Huc, M., ... & Roujean, J. L. (2007). LAI, fAPAR and fCover CYCLOPES global products derived from VEGETATION: Part 1: Principles of the algorithm. Remote sensing of environment, 110(3), 275-286.

Bastos, A., Friedlingstein, P., Sitch, S., Chen, C., Mialon, A., Wigneron, J. P., ... & Chevallier, F. (2018). Impact of the 2015/2016 El Niño on the terrestrial carbon cycle constrained by bottom-up and top-down approaches. Philosophical Transactions of the Royal Society B: Biological Sciences, 373(1760), 20170304.

Baur, M. J., Jagdhuber, T., Feldman, A. F., Akbar, R., & Entekhabi, D. (2019). Estimation of relative canopy absorption and scattering at L-, C-and X-bands. Remote Sensing of Environment, 233, 111384.

Beck, H. E., Pan, M., Miralles, D. G., Reichle, R. H., Dorigo, W. A., Hahn, S., ... & van Dijk, A. I. (2020). Evaluation of 18 satellite-and model-based soil moisture products using in situ measurements from 826 sensors. Hydrology and Earth System Sciences Discussions, 1-35.

Becker, F., & Choudhury, B. J. (1988). Relative sensitivity of normalized difference vegetation index (NDVI) and microwave polarization difference index (MPDI) for vegetation and desertification monitoring. Remote Sensing of Environment, 24(2), 297-311.

833 Bouvet, A., Mermoz, S., Le Toan, T., Villard, L., Mathieu, R., Naidoo, L., & Asner, G. P.
834 (2018). An above-ground biomass map of African savannahs and woodlands at 25 m
835 resolution derived from ALOS PALSAR. Remote sensing of environment, 206, 156-173.
836 Brandt, M., Wigneron, J. P., Chave, J., Tagesson, T., Penuelas, J., Ciais, P., ... & Rodriguez-
837 Fernandez, N. (2018a). Satellite passive microwaves reveal recent climate-induced carbon
838 losses in African drylands. Nature ecology & evolution, 2(5), 827-835. doi:
839 10.1038/s41559-018-0530-6
840 Brandt, M., Yue, Y., Wigneron, J. P., Tong, X., Tian, F., Jepsen, M. R., ... & Wang, K. (2018b).
841 Satellite‐observed major greening and biomass increase in south China karst during recent
842 decade. Earth's Future, 6(7), 1017-1028. doi: 10.1029/2018ef000890
843 Buchhorn, M., Bertels, L., Smets, B., Lesiv, M., & Wur, N. E. T. (2017). Copernicus Global
844 Land Operations "Vegetation and Energy".
845 C3S: ERA5-Land reanalysis, https://cds.climate.copernicus.eu, 2019.
846 Carreiras, J. M., Quegan, S., Le Toan, T., Minh, D. H. T., Saatchi, S. S., Carvalhais, N., ... &
847 Scipal, K. (2017). Coverage of high biomass forests by the ESA BIOMASS mission under
848 defense restrictions. Remote Sensing of Environment, 196, 154-162. doi:
849 10.1016/j.rse.2017.05.003
850 Chaparro, D., Duveiller, G., Piles, M., Cescatti, A., Vall-Llossera, M., Camps, A., & Entekhabi,
851 D. (2019). Sensitivity of L-band vegetation optical depth to carbon stocks in tropical forests:
852 a comparison to higher frequencies and optical indices. Remote sensing of environment,
853 232, 111303. doi: 10.1016/j.rse.2019.111303
854 Chaparro, D., Piles, M., Vall-Llossera, M., Camps, A., Konings, A. G., & Entekhabi, D. (2018).
855 L-band vegetation optical depth seasonal metrics for crop yield assessment. Remote
856 Sensing of Environment, 212, 249-259. doi: 10.1016/j.rse.2018.04.049

857 Chaubell, M. J., Yueh, S. H., Dunbar, R. S., Colliander, A., Chen, F., Chan, S. K., ... & Berg,
858 A. A. (2020). Improved SMAP Dual-Channel Algorithm for the Retrieval of Soil Moisture.
859 IEEE Transactions on Geoscience and Remote Sensing, 58(6), 3894-3905. doi:
860 10.1109/tgrs.2019.2959239
861 Chen, Y., Feng, X., & Fu, B. (2021). An improved global remote-sensing-based surface soil
862 moisture (RSSSM) dataset covering 2003–2018. Earth System Science Data, 13(1), 1-31.
863 doi.org/10.5194/essd-13-1-2021
864 Choudhury, B. J., Schmugge, T. J., Chang, A., & Newton, R. W. (1979). Effect of surface
865 roughness on the microwave emission from soils. Journal of Geophysical Research: Oceans,
866 84(C9), 5699-5706. doi: 10.1029/JC084iC09p05699
867 Choudhury, B. J., Schmugge, T. J., & Mo, T. (1982). A parameterization of effective soil
868 temperature for microwave emission. Journal of Geophysical Research: Oceans, 87(C2),
869 1301-1304. doi: 10.1029/JC087iC02p01301
870 Cui, C., Xu, J., Zeng, J., Chen, K. S., Bai, X., Lu, H., ... & Zhao, T. (2018). Soil moisture
871 mapping from satellites: An intercomparison of SMAP, SMOS, FY3B, AMSR2, and ESA
872 CCI over two dense network regions at different spatial scales. Remote Sensing, 10(1), 33.
873 Della Vecchia, A., Ferrazzoli, P., Guerriero, L., Rahmoune, R., Paloscia, S., Pettinato, S., &
874 Santi, E. (2009). Modeling the multifrequency emission of broadleaf forests and their
875 components. IEEE transactions on geoscience and remote sensing, 48(1), 260-272. doi:
876 10.1109/TGRS.2009.2029343
877 de Nijs, A. H., Parinussa, R. M., de Jeu, R. A., Schellekens, J., & Holmes, T. R. (2015). A
878 methodology to determine radio-frequency interference in AMSR2 observations. IEEE
879 Transactions on Geoscience and Remote Sensing, 53(9), 5148-5159. doi:
880 10.1109/tgrs.2015.2417653

881 Draper, D. W. (2018). Radio frequency environment for Earth-observing passive microwave
882 imagers. IEEE Journal of Selected Topics in Applied Earth Observations and Remote
883 Sensing, 11(6), 1913-1922. doi: 10.1109/jstars.2018.2801019
884 Du, J., Kimball, J. S., & Jones, L. A. (2015). Passive microwave remote sensing of soil moisture
885 based on dynamic vegetation scattering properties for AMSR-E. IEEE Transactions on
886 Geoscience and Remote Sensing, 54(1), 597-608. doi: 10.1109/tgrs.2015.2462758
887 Du, J., Kimball, J. S., Jones, L. A., Kim, Y., Glassy, J. M., & Watts, J. D. (2017). A global
888 satellite environmental data record derived from AMSR-E and AMSR2 microwave Earth
889 observations. Earth System Science Data, 9, 791-808. doi: 10.5194/essd-9-791-2017
890 Fan, L., Wigneron, J. P., Ciais, P., Chave, J., Brandt, M., Fensholt, R., ... & Qin, Y. (2019).
891 Satellite-observed pantropical carbon dynamics. Nature plants, 5(9), 944-951. doi:
892 10.1038/s41477-019-0478-9
893 Feldman, A. F., Akbar, R., & Entekhabi, D. (2018). Characterization of higher-order scattering
894 from vegetation with SMAP measurements. Remote sensing of environment, 219, 324-338.
895 doi: 10.1016/j.rse.2018.10.022
896 Feldman, A. F., Gianotti, D. J. S., Konings, A. G., McColl, K. A., Akbar, R., Salvucci, G. D.,
897 & Entekhabi, D. (2018). Moisture pulse-reserve in the soil-plant continuum observed across
898 biomes. Nature plants, 4(12), 1026-1033. doi: 10.1038/s41477-018-0304-9
899 Feldman, A. F., Short Gianotti, D. J., Konings, A. G., Gentine, P., & Entekhabi, D. (2020).
900 Patterns of plant rehydration and growth following pulses of soil moisture availability.
901 Biogeosciences Discussions, 1-24.
902 Fernandez-Moran, R., Al-Yaari, A., Mialon, A., Mahmoodi, A., Al Bitar, A., De Lannoy, G., ...
903 & Wigneron, J. P. (2017). SMOS-IC: An alternative SMOS soil moisture and vegetation
904 optical depth product. Remote Sensing, 9(5), 457. doi: 10.3390/rs9050457

905 Frappart, F., Wigneron, J. P., Li, X., Liu, X., Al-Yaari, A., Fan, L., ... & Vallé, C. (2020). Global
906 monitoring of the vegetation dynamics from the Vegetation Optical Depth (VOD): A
907 review. Remote Sensing, 12(18), 2915. doi: 10.3390/rs12182915
908 Friedl, M., Sulla-Menashe, D. (2019). MCD12Q1 MODIS/Terra+Aqua Land Cover Type
909 Yearly L3 Global 500m SIN Grid V006 [Data set]. NASA EOSDIS Land Processes DAAC.
910 Accessed 2021-05-19 from https://doi.org/10.5067/MODIS/MCD12Q1.006
911 Fujii, H., Koike, T., & Imaoka, K. (2009). Improvement of the AMSR-E algorithm for soil
912 moisture estimation by introducing a fractional vegetation coverage dataset derived from
913 MODIS data. Journal of the remote sensing society of Japan, 29(1), 282-292. doi:
914 10.11440/rssj.29.282
915 Gao, L., Sadeghi, M., & Ebtehaj, A. (2020). Microwave retrievals of soil moisture and
916 vegetation optical depth with improved resolution using a combined constrained inversion
917 algorithm: Application for SMAP satellite. Remote Sensing of Environment, 239, 111662.
918 doi: 10.1016/j.rse.2020.111662
919 Gevaert, A. I., Parinussa, R. M., Renzullo, L. J., van Dijk, A. I., & de Jeu, R. A. (2016). Spatio-
920 temporal evaluation of resolution enhancement for passive microwave soil moisture and
921 vegetation optical depth. International journal of applied earth observation and
922 geoinformation, 45, 235-244. doi: 10.1016/j.jag.2015.08.006
923 Guan, K., Wu, J., Kimball, J. S., Anderson, M. C., Frolking, S., Li, B., ... & Lobell, D. B. (2017).
924 The shared and unique values of optical, fluorescence, thermal and microwave satellite data
925 for estimating large-scale crop yields. Remote sensing of environment, 199, 333-349. doi:
926 10.1016/j.rse.2017.06.043
927 Gupta, V. K., Sharma, N., & Jangid, R. A. (2013). Emission and scattering behaviour of bare
928 and vegetative soil surfaces of different moist states by microwave remote sensing. Indian
929 Journal of Radio & Space Physics 42: 42-51.

930 Hamilton, S. E., & Friess, D. A. (2018). Global carbon stocks and potential emissions due to
931 mangrove deforestation from 2000 to 2012. Nature Climate Change, 8(3), 240-244. doi:
932 10.1038/s41558-018-0090-4
933 Hersbach, H., Bell, B., Berrisford, P., Hirahara, S., Horányi, A., Muñoz‐Sabater, J., ... &
934 Simmons, A. (2020). The ERA5 global reanalysis. Quarterly Journal of the Royal
935 Meteorological Society, 146(730), 1999-2049. doi: 10.1002/qj.3803
936 Hornbuckle, B. K., Patton, J. C., VanLoocke, A., Suyker, A. E., Roby, M. C., Walker, V. A., ...
937 & Endacott, E. A. (2016). SMOS optical thickness changes in response to the growth and
938 development of crops, crop management, and weather. Remote Sensing of Environment,
939 180, 320-333. doi: 10.1016/j.rse.2016.02.043
940 Jackson, T. J. (1993). III. Measuring surface soil moisture using passive microwave remote
941 sensing. Hydrological processes, 7(2), 139-152.
942 JAXA. (2013). Data users' manual for the advanced microwave scanning radiometer 2
943 (AMSR2) onboard the global change observation mission 1st—water "SHIZUKU"
944 (GCOM‐W1).
945 Jones, M. O., Jones, L. A., Kimball, J. S., & McDonald, K. C. (2011). Satellite passive
946 microwave remote sensing for monitoring global land surface phenology. Remote Sensing
947 of Environment, 115(4), 1102-1114. doi: 10.1016/j.rse.2010.12.015
948 Jones, M. O., Kimball, J. S., Jones, L. A., & McDonald, K. C. (2012). Satellite passive
949 microwave detection of North America start of season. Remote Sensing of Environment,
950 123, 324-333. doi: 10.1016/j.rse.2012.03.025
951 Jones, M. O., Kimball, J. S., & Nemani, R. R. (2014). Asynchronous Amazon forest canopy
952 phenology indicates adaptation to both water and light availability. Environmental
953 Research Letters, 9(12), 124021. doi: 10.1088/1748-9326/9/12/124021

954 Jackson, T. J., & Schmugge, T. J. (1991). Vegetation effects on the microwave emission of
955 soils. Remote Sensing of Environment, 36(3), 203-212. doi: 10.1016/0034-4257(91)90057-
956 D
957 Karthikeyan, L., Pan, M., Konings, A. G., Piles, M., Fernandez-Moran, R., Kumar, D. N., &
958 Wood, E. F. (2019). Simultaneous retrieval of global scale Vegetation Optical Depth,
959 surface roughness, and soil moisture using X-band AMSR-E observations. Remote Sensing
960 of Environment, 234, 111473. doi: 10.1016/j.rse.2019.111473
961 Kerr, Y. H., Waldteufel, P., Richaume, P., Wigneron, J. P., Ferrazzoli, P., Mahmoodi, A., ... &
962 Leroux, D. (2012). The SMOS soil moisture retrieval algorithm. IEEE transactions on
963 geoscience and remote sensing, 50(5), 1384-1403. doi: 10.1109/tgrs.2012.2184548
964 Koike, T. (1996). Spatial and seasonal distribution of surface wetness derived from satellite
965 data. In Proc. of the Int'l Workshop on Macro-Scale Hydrological Modeling (pp. 87-90).
966 Koike, T., Nakamura, Y., Kaihotsu, I., Davaa, G., Matsuura, N., Tamagawa, K., & Fujii, H.
967 (2004). Development of an advanced microwave scanning radiometer (AMSR-E)
968 algorithm for soil moisture and vegetation water content. Proceedings of Hydraulic
969 Engineering, 48, 217-222.
970 Konings, A. G., & Gentine, P. (2017). Global variations in ecosystem ‐ scale isohydricity.
971 Global change biology, 23(2), 891-905. doi: 10.1111/gcb.13389
972 Konings, A. G., Piles, M., Das, N., & Entekhabi, D. (2017a). L-band vegetation optical depth
973 and effective scattering albedo estimation from SMAP. Remote Sensing of Environment,
974 198, 460-470. doi: 10.1016/j.rse.2017.06.037
975 Konings, A. G., Piles, M., Rötzer, K., McColl, K. A., Chan, S. K., & Entekhabi, D. (2016).
976 Vegetation optical depth and scattering albedo retrieval using time series of dual-polarized
977 L-band radiometer observations. Remote sensing of environment, 172, 178-189. doi:
978 10.1016/j.rse.2015.11.009

979 Konings, A. G., Yu, Y., Xu, L., Yang, Y., Schimel, D. S., & Saatchi, S. S. (2017b). Active
980 microwave observations of diurnal and seasonal variations of canopy water content across
981 the humid African tropical forests. Geophysical Research Letters, 44(5), 2290-2299. doi:
982 10.1002/2016GL072388
983 Kumar, S. V., Holmes, T. R., Bindlish, R., Jeu, R. D., & Peters-Lidard, C. (2020). Assimilation
984 of vegetation optical depth retrievals from passive microwave radiometry. Hydrology and
985 Earth System Sciences, 24(7), 3431-3450. doi: 10.5194/hess-24-3431-2020
986 Kurum, M. (2013). Quantifying scattering albedo in microwave emission of vegetated terrain.
987 Remote Sensing of Environment, 129, 66-74. doi: 10.1016/j.rse.2012.10.021
988 Lacava, T., Faruolo, M., Pergola, N., Coviello, I., & Tramutoli, V. (2012, March). A
989 comprehensive analysis of AMSRE C-and X-bands Radio Frequency Interferences. In
990 2012 12th Specialist Meeting on Microwave Radiometry and Remote Sensing of the
991 Environment (MicroRad) (pp. 1-4). IEEE.
992 Li, X., Wigneron, J. P., Frappart, F., Fan, L., Ciais, P., Fensholt, R., ... & Moisy, C. (2021)
993 Global-scale assessment and inter-comparison of recently developed/reprocessed
994 microwave satellite vegetation optical depth products. Remote Sensing of Environment,
995 253, 112208. doi: 10.1016/j.rse.2020.112208
996 Li, M., Wu, P., & Ma, Z. (2020). A comprehensive evaluation of soil moisture and soil
997 temperature from third‐generation atmospheric and land reanalysis data sets. International
998 Journal of Climatology, 40, 5744-5766. doi: 10.1002/joc.6549
999 Liu, Y. Y., Evans, J. P., McCabe, M. F., De Jeu, R. A., van Dijk, A. I., Dolman, A. J., & Saizen,
1000 I. (2013). Changing climate and overgrazing are decimating Mongolian steppes. PloS one,
1001 8(2), e57599. doi: 10.1371/journal.pone.0057599Liu, Y. Y., Van Dijk, A. I., De Jeu, R. A.,
1002 Canadell, J. G., McCabe, M. F., Evans, J. P., & Wang, G. (2015). Recent reversal in loss

of global terrestrial biomass. Nature Climate Change, 5(5), 470-474. doi: 10.1038/nclimate2581

Liu, Y. Y., van Dijk, A. I., Miralles, D. G., McCabe, M. F., Evans, J. P., de Jeu, R. A., ... & Restrepo-Coupe, N. (2018). Enhanced canopy growth precedes senescence in 2005 and 2010 Amazonian droughts. Remote Sensing of Environment, 211, 26-37. doi: 10.1016/j.rse.2018.03.035

Long, D., Bai, L., Yan, L., Zhang, C., Yang, W., Lei, H., ... & Shi, C. (2019). Generation of spatially complete and daily continuous surface soil moisture of high spatial resolution. Remote Sensing of Environment, 233, 111364.

Long, D., Yan, L., Bai, L., Zhang, C., Li, X., Lei, H., ... & Shi, C. (2020). Generation of MODIS-like land surface temperatures under all-weather conditions based on a data fusion approach. Remote Sensing of Environment, 246, 111863.

Ma, H., Zeng, J., Chen, N., Zhang, X., Cosh, M. H., & Wang, W. (2019). Satellite surface soil moisture from SMAP, SMOS, AMSR2 and ESA CCI: A comprehensive assessment using global ground-based observations. Remote Sensing of Environment, 231, 111215.

Mateo-Sanchis, A., Piles, M., Muñoz-Marí, J., Adsuara, J. E., Pérez-Suay, A., & Camps-Valls, G. (2019). Synergistic integration of optical and microwave satellite data for crop yield estimation. Remote sensing of environment, 234, 111460. doi: 10.1016/j.rse.2019.111460

Meesters, A. G., De Jeu, R. A., & Owe, M. (2005). Analytical derivation of the vegetation optical depth from the microwave polarization difference index. IEEE Geoscience and Remote Sensing Letters, 2(2), 121-123. doi: 10.1109/lgrs.2005.843983

Mermoz, S., Réjou-Méchain, M., Villard, L., Le Toan, T., Rossi, V., & Gourlet-Fleury, S. (2015). Decrease of L-band SAR backscatter with biomass of dense forests. Remote Sensing of Environment, 159, 307-317. doi: 10.1016/j.rse.2014.12.019

1027 Mironov, V., Kerr, Y., Wigneron, J. P., Kosolapova, L., & Demontoux, F. (2012). Temperature-
1028 and texture-dependent dielectric model for moist soils at 1.4 GHz. IEEE Geoscience and
1029 Remote Sensing Letters, 10(3), 419-423. doi: 10.1109/lgrs.2012.2207878
1030 Mladenova, I. E., Jackson, T. J., Njoku, E., Bindlish, R., Chan, S., Cosh, M. H., ... & Santi, E.
1031 (2014). Remote monitoring of soil moisture using passive microwave-based techniques—
1032 Theoretical basis and overview of selected algorithms for AMSR-E. Remote sensing of
1033 environment, 144, 197-213. doi: 10.1016/j.rse.2014.01.013
1034 Mo, T., Choudhury, B. J., Schmugge, T. J., Wang, J. R., & Jackson, T. J. (1982). A model for
1035 microwave emission from vegetation ‐ covered fields. Journal of Geophysical Research:
1036 Oceans, 87(C13), 11229-11237. doi: 10.1029/JC087iC13p11229
1037 Moesinger, L., Dorigo, W., de Jeu, R., van der Schalie, R., Scanlon, T., Teubner, I., & Forkel,
1038 M. (2020). The global long-term microwave Vegetation Optical Depth Climate Archive
1039 (VODCA). Earth System Science Data, 12(1), 177-196. doi: 10.5194/essd-12-177-2020
1040 Montpetit, B., Royer, A., Wigneron, J. P., Chanzy, A., & Mialon, A. (2015). Evaluation of
1041 multi-frequency bare soil microwave reflectivity models. Remote Sensing of Environment,
1042 162, 186-195. doi: 10.1016/j.rse.2015.02.015
1043 Morton, D. C., Nagol, J., Carabajal, C. C., Rosette, J., Palace, M., Cook, B. D., ... & North, P.
1044 R. (2014). Amazon forests maintain consistent canopy structure and greenness during the
1045 dry season. Nature, 506(7487), 221-224.
1046 Njoku, E. G., Ashcroft, P., Chan, T. K., & Li, L. (2005). Global survey and statistics of radio-
1047 frequency interference in AMSR-E land observations. IEEE Transactions on Geoscience
1048 and Remote Sensing, 43(5), 938-947. doi: 10.1109/tgrs.2004.837507
1049 Njoku, E. G., & Chan, S. K. (2006). Vegetation and surface roughness effects on AMSR-E land
1050 observations. Remote Sensing of environment, 100(2), 190-199.

1051 O'Neill, P., Chan, S., Njoku, E., Jackson, T., & Bindlish, R. (2015). Soil moisture active passive
1052 (SMAP) algorithm theoretical basis document Level 2 & 3 soil moisture (passive) data
1053 products. Jet Propulsion Laboratory, NASA: Pasadena, CA, USA.
1054 Owe, M., Holmes, T., & De Jeu, R. (2005, October). A physically-based model with remote
1055 sensing inputs for improved soil temperature retrievals. In Remote Sensing for Agriculture,
1056 Ecosystems, and Hydrology VII (Vol. 5976, p. 59760N). International Society for Optics
1057 and Photonics.
1058 Owe, M., de Jeu, R., & Holmes, T. (2008). Multisensor historical climatology of satellite -
1059 derived global land surface moisture. Journal of Geophysical Research: Earth Surface,
1060 113(F1). doi: 10.1029/2007jf000769
1061 Owe, M., de Jeu, R., & Walker, J. (2001). A methodology for surface soil moisture and
1062 vegetation optical depth retrieval using the microwave polarization difference index. IEEE
1063 Transactions on Geoscience and Remote Sensing, 39(8), 1643-1654.
1064 Paloscia, S., Macelloni, G., & Santi, E. (2006). Soil moisture estimates from AMSR-E
1065 brightness temperatures by using a dual-frequency algorithm. IEEE Transactions on
1066 Geoscience and Remote Sensing, 44(11), 3135-3144. doi: 10.1109/TGRS.2006.881714
1067 Paloscia, S., Macelloni, G., Santi, E., & Koike, T. (2001). A multifrequency algorithm for the
1068 retrieval of soil moisture on a large scale using microwave data from SMMR and SSM/I
1069 satellites. IEEE Transactions on Geoscience and Remote Sensing, 39(8), 1655-1661. doi:
1070 10.1109/36.942543Paloscia, S., & Pampaloni, P. (1988). Microwave polarization index for
1071 monitoring vegetation growth. IEEE Transactions on Geoscience and Remote Sensing,
1072 26(5), 617-621. doi: 10.1109/36.7687
1073 Paloscia, S., & Pampaloni, P. (1992). Microwave vegetation indexes for detecting biomass and
1074 water conditions of agricultural crops. Remote sensing of environment, 40(1), 15-26. doi:
1075 10.1016/0034-4257(92)90123-2

Paloscia, S., Pampaloni, P., Chiarantini, L., Coppo, P., Gagliani, S., & Luzi, G. (1993). Multifrequency passive microwave remote sensing of soil moisture and roughness. International Journal of Remote Sensing, 14(3), 467-483. doi: 10.1080/01431169308904351

Pampaloni, P., & Paloscia, S. (1985). Experimental relationships between microwave emission and vegetation features. International Journal of Remote Sensing, 6(2), 315-323. doi: 10.1080/01431168508948446

Pampaloni, P., & Paloscia, S. (1986). Microwave emission and plant water content: A comparison between field measurements and theory. IEEE Transactions on Geoscience and Remote Sensing, (6), 900-905. doi: 10.1109/TGRS.1986.289705

Pan, M., Sahoo, A. K., & Wood, E. F. (2014). Improving soil moisture retrievals from a physically-based radiative transfer model. Remote Sensing of Environment, 140, 130-140. doi: 10.1016/j.rse.2013.08.020

Pan, Y., Li, L., Jiang, X., Li, G., Zhang, W., Wang, X., & Ingersoll, A. P. (2017). Earth's changing global atmospheric energy cycle in response to climate change. Nature communications, 8(1), 1-8. doi: 10.1038/ncomms14367

Pellarin, T., Kerr, Y. H., & Wigneron, J. P. (2006). Global simulation of brightness temperatures at 6.6 and 10.7 GHz over land based on SMMR data set analysis. IEEE Transactions on Geoscience and Remote Sensing, 44(9), 2492-2505. doi: 10.1109/tgrs.2006.874139

Peng, J., Albergel, C., Balenzano, A., Brocca, L., Cartus, O., Cosh, M. H., ... & Loew, A. (2020). A roadmap for high-resolution satellite soil moisture applications–confronting product characteristics with user requirements. Remote Sensing of Environment, 112162.

1099 Qin, Y., Xiao, X., Wigneron, J. P., Ciais, P., Brandt, M., Fan, L., ... & Moore, B. (2021). Carbon
1100 loss from forest degradation exceeds that from deforestation in the Brazilian Amazon.
1101 Nature Climate Change, 1-7. https://doi.org/10.1038/s41558-021-01026-5
1102 Rao, K., Anderegg, W. R., Sala, A., Martínez-Vilalta, J., & Konings, A. G. (2019). Satellite-
1103 based vegetation optical depth as an indicator of drought-driven tree mortality. Remote
1104 Sensing of Environment, 227, 125-136. doi: 10.1016/j.rse.2019.03.026
1105 Rodríguez-Fernández, N. J., Mialon, A., Mermoz, S., Bouvet, A., Richaume, P., Al Bitar, A., ...
1106 & Kerr, Y. H. (2018). An evaluation of SMOS L-band vegetation optical depth (L-VOD)
1107 data sets: high sensitivity of L-VOD to above-ground biomass in Africa. Biogeosciences,
1108 15(14), 4627-4645. doi: 10.5194/bg-15-4627-2018
1109 Saatchi, S. S., Harris, N. L., Brown, S., Lefsky, M., Mitchard, E. T., Salas, W., ... & Petrova, S.
1110 (2011). Benchmark map of forest carbon stocks in tropical regions across three continents.
1111 Proceedings of the national academy of sciences, 108(24), 9899-9904. doi:
1112 10.1073/pnas.1019576108
1113 Sabaghy, S., Walker, J. P., Renzullo, L. J., Akbar, R., Chan, S., Chaubell, J., ... & Yueh, S.
1114 (2020). Comprehensive analysis of alternative downscaled soil moisture products. Remote
1115 Sensing of Environment, 239, 111586. doi: 10.1016/j.rse.2019.111586
1116 Santi, E. (2010). An application of the SFIM technique to enhance the spatial resolution of
1117 spaceborne microwave radiometers. International Journal of Remote Sensing, 31(9), 2419-
1118 2428. doi: 10.1080/01431160903005725
1119 Santi, E., Paloscia, S., Pampaloni, P., & Pettinato, S. (2009). Ground-based microwave
1120 investigations of forest plots in Italy. IEEE Transactions on Geoscience and Remote
1121 Sensing, 47(9), 3016-3025. doi: 10.1109/TGRS.2009.2021613

Santoro, M.; Cartus, O. (2019): ESA Biomass Climate Change Initiative (Biomass_cci): Global datasets of forest above-ground biomass for the year 2017, v1. Centre for Environmental Data Analysis, 02 December 2019. doi:10.5285/bedc59f37c9545c981a839eb552e4084.

Schmugge, T. J., & Choudhury, B. J. (1981). A comparison of radiative transfer models for predicting the microwave emission from soils. Radio Science, 16(05), 927-938. doi: 10.1029/RS016i005p00927

Shi, J., Jackson, T., Tao, J., Du, J., Bindlish, R., Lu, L., & Chen, K. S. (2008). Microwave vegetation indices for short vegetation covers from satellite passive microwave sensor AMSR-E. Remote sensing of environment, 112(12), 4285-4300. doi: 10.1016/j.rse.2008.07.015

Swinnen, E., & Toté, C. (2017). Gio Global Land Component–Lot I "Operation of the Global Land Component", Framework Service Contract N 388533 (JRC), Algorithm Theoretical Basis Document, Normalized Difference Vegetation Index (NDVI), Collection 1km, Version 2.2. Document-No. GIOGL1_ATBD_NDVI1km-V2, (I2), 21.

Teubner, I. E., Forkel, M., Camps-Valls, G., Jung, M., Miralles, D. G., Tramontana, G., ... & Dorigo, W. A. (2019). A carbon sink-driven approach to estimate gross primary production from microwave satellite observations. Remote Sensing of Environment, 229, 100-113. doi: 10.1016/j.rse.2019.04.022

Teubner, I. E., Forkel, M., Jung, M., Liu, Y. Y., Miralles, D. G., Parinussa, R., ... & Dorigo, W. A. (2018). Assessing the relationship between microwave vegetation optical depth and gross primary production. International journal of applied earth observation and geoinformation, 65, 79-91. doi: 10.1016/j.jag.2017.10.006

Tian, F., Brandt, M., Liu, Y. Y., Verger, A., Tagesson, T., Diouf, A. A., ... & Fensholt, R. (2016). Remote sensing of vegetation dynamics in drylands: Evaluating vegetation optical

depth (VOD) using AVHRR NDVI and in situ green biomass data over West African Sahel. Remote Sensing of Environment, 177, 265-276. doi: 10.1016/j.rse.2016.02.056

Tian, F., Wigneron, J. P., Ciais, P., Chave, J., Ogée, J., Penuelas, J., ... & Mialon, A. (2018). Coupling of ecosystem-scale plant water storage and leaf phenology observed by satellite. Nature ecology & evolution, 2(9), 1428-1435. doi: 10.1038/s41559-018-0630-3

Tong, X., Brandt, M., Yue, Y., Ciais, P., Jepsen, M. R., Penuelas, J., ... & Rasmussen, K. (2020). Forest management in southern China generates short term extensive carbon sequestration. Nature communications, 11(1), 1-10. doi: 10.1038/s41467-019-13798-8

Tong, X., Tian, F., Brandt, M., Liu, Y., Zhang, W., & Fensholt, R. (2019). Trends of land surface phenology derived from passive microwave and optical remote sensing systems and associated drivers across the dry tropics 1992–2012. Remote Sensing of Environment, 232, 111307. doi: 10.1016/j.rse.2019.111307

Ulaby, F. T., Moore, R. K., & Fung, A. K. (1986). Microwave remote sensing: Active and passive. Volume 3-From theory to applications.

Van de Griend, A. A., Owe, M., de Ruiter, J., & Gouweleeuw, B. T. (1996). Measurement and behavior of dual-polarization vegetation optical depth and single scattering albedo at 1.4- and 5-GHz microwave frequencies. IEEE Transactions on Geoscience and Remote Sensing, 34(4), 957-965.

Vittucci, C., Laurin, G. V., Tramontana, G., Ferrazzoli, P., Guerriero, L., & Papale, D. (2019). Vegetation optical depth at L-band and above ground biomass in the tropical range: Evaluating their relationships at continental and regional scales. International Journal of Applied Earth Observation and Geoinformation, 77, 151-161. doi: 10.1016/j.jag.2019.01.006

Wang, S., Wigneron, J. P., Jiang, L. M., Parrens, M., Yu, X. Y., Al-Yaari, A., ... & Kerr, Y. (2015). Global-scale evaluation of roughness effects on C-band AMSR-E observations. Remote Sensing, 7(5), 5734-5757. doi: 10.3390/rs70505734

Wigneron, J. P., Chanzy, A., Calvet, J. C., & Bruguier, N. (1995). A simple algorithm to retrieve soil moisture and vegetation biomass using passive microwave measurements over crop fields. Remote Sensing of Environment, 51(3), 331-341.

Wigneron, J. P., Chanzy, A., de Rosnay, P., Rudiger, C., & Calvet, J. C. (2008). Estimating the effective soil temperature at L-band as a function of soil properties. IEEE Transactions on Geoscience and Remote Sensing, 46(3), 797-807. doi: 10.1109/tgrs.2007.914806

Wigneron, J. P., Fan, L., Ciais, P., Bastos, A., Brandt, M., Chave, J., ... & Fensholt, R. (2020). Tropical forests did not recover from the strong 2015–2016 El Niño event. Science advances, 6(6), eaay4603.

Wigneron, J. P., Jackson, T. J., O'neill, P., De Lannoy, G., De Rosnay, P., Walker, J. P., ... & Kurum, M. (2017). Modelling the passive microwave signature from land surfaces: A review of recent results and application to the L-band SMOS & SMAP soil moisture retrieval algorithms. Remote Sensing of Environment, 192, 238-262. doi: 10.1016/j.rse.2017.01.024

Wigneron, J. P., Kerr, Y., Waldteufel, P., Saleh, K., Escorihuela, M. J., Richaume, P., ... & Grant, J. P. (2007). L-band microwave emission of the biosphere (L-MEB) model: Description and calibration against experimental data sets over crop fields. Remote Sensing of Environment, 107(4), 639-655. doi: 10.1016/j.rse.2006.10.014

Wigneron, J. P., Pardé, M., Waldteufel, P., Chanzy, A., Kerr, Y., Schmidl, S., & Skou, N. (2004). Characterizing the dependence of vegetation model parameters on crop structure, incidence angle, and polarization at L-band. IEEE Transactions on Geoscience and Remote Sensing, 42(2), 416-425. doi: 10.1109/tgrs.2003.817976

Wigneron, J. P., Li, X., Frappart, F., Fan, L., Al-Yaari, A., De Lannoy, G., ... & Moisy, C. SMOS-IC data record of soil moisture and L-VOD: Historical development, applications and perspectives. Remote Sensing of Environment, 254, 112238. doi: 10.1016/j.rse.2020.112238

Yang, K., Koike, T., Ye, B., & Bastidas, L. (2005). Inverse analysis of the role of soil vertical heterogeneity in controlling surface soil state and energy partition. Journal of Geophysical Research: Atmospheres, 110(D8). doi: 10.1029/2004JD005500

Yang, K., Watanabe, T., Koike, T., Li, X., FUJII, H., Tamagawa, K., ... & Ishikawa, H. (2007). Auto-calibration system developed to assimilate AMSR-E data into a land surface model for estimating soil moisture and the surface energy budget. Journal of the Meteorological Society of Japan. Ser. II, 85, 229-242. doi: 10.2151/jmsj.85A.229

Zeng, J., Li, Z., Chen, Q., & Bi, H. (2014). Method for soil moisture and surface temperature estimation in the Tibetan Plateau using spaceborne radiometer observations. IEEE Geoscience and Remote Sensing Letters, 12(1), 97-101.Zhang, Y., Zhou, S., Gentine, P., & Xiao, X. (2019). Can vegetation optical depth reflect changes in leaf water potential during soil moisture dry-down events?. Remote Sensing of Environment, 234, 111451. doi: 10.1016/j.rse.2019.111451

Zhao, T., Hu, L., Shi, J., Lü, H., Li, S., Fan, D., ... & Zhang, Z. (2020). Soil moisture retrievals using L-band radiometry from variable angular ground-based and airborne observations. Remote Sensing of Environment, 248, 111958.

Zhao, T., Shi, J., Entekhabi, D., Jackson, T. J., Hu, L., Peng, Z., ... & Kang, C. S. (2021). Retrievals of soil moisture and vegetation optical depth using a multi-channel collaborative algorithm. Remote Sensing of Environment, 257, 112321.

Zhou, X., Yamaguchi, Y., & Arjasakusuma, S. (2018). Distinguishing the vegetation dynamics induced by anthropogenic factors using vegetation optical depth and AVHRR NDVI: A

1219 cross-border study on the Mongolian Plateau. Science of the Total Environment, 616, 730-
1220 743. doi: 10.1016/j.scitotenv.2017.10.253
1221
1222
1223
1224